INTERNATIONAL JOURNAL FOR NUMERICAL METHODS IN ENGINEERING
Int. J. Numer. Meth. Engng 2011; **00**:1–45
Published online in Wiley InterScience (www.interscience.wiley.com). DOI: 10.1002/nme

A full-discontinuous Galerkin formulation of non-linear Kirchhoff-Love shells: elasto-plastic finite deformations, parallel computation & fracture applications

G. Becker[†], L. Noels[‡,*]

University of Liège, Computational & Multiscale Mechanics of Materials,
Chemin des Chevreuils 1, B-4000 Liège, Belgium

SUMMARY

Due to its ability to take into account discontinuities, the discontinuous Galerkin (DG) method presents some advantages for modeling crack initiations and propagations. This concept has been recently applied to 3D simulations and to elastic thin bodies. In this last case, the assumption of small elastic deformations before crack initiations or propagations reduces drastically the applicability of the framework to a reduced number of materials.
To remove this limitation, a full-DG formulation of non-linear Kirchhoff-Love shells is presented and is used in combination with an elasto-plastic finite deformations model. The results obtained by this new formulation are in agreement with other continuum elasto-plastic shell formulations.
Then this full-DG formulation of Kirchhoff-Love shells is coupled with the cohesive zone model to perform thin body fracture simulations. As this method allows considering elasto-plastic constitutive laws in combination with the cohesive model, accurate results compared to the experiments are found. In particular, the crack path and propagation rate of a blasted cylinder are shown to match experimental results. One of the main advantages of this framework is its ability to run in parallel with a high speed-up factor, allowing the simulation of ultra fine meshes. Copyright © 2011 John Wiley & Sons, Ltd.

Received . . .

KEY WORDS: Finite element methods; Fracture; Discontinuous Galerkin; Shells; Plasticity; Extrinsic Cohesive Law

1. INTRODUCTION

The tearing prediction of thin structures is a challenging task which can be numerically investigated using cohesive models. Such a cohesive model was pioneered by A. Hillerborg *et al.* [1] who presented a numerical implementation of the work of D. Dugdale [2] and G. Barenblatt [3]. These works suggested to model the fracture process by defining a cohesive zone located ahead from the crack tip where the traction surface at the lips is related to the opening by a "Traction Separation

[†]PhD candidate at the Belgian National Fund for Education at the Research in Industry and Farming
[‡]University of Liége, department of Aerospace and Mechanical Engineering Department, CM3.
[*]Correspondence to: L.Noels@ulg.ac.be

Law" (TSL), whose shape depends on the fracture nature. In order to study the debonding of a

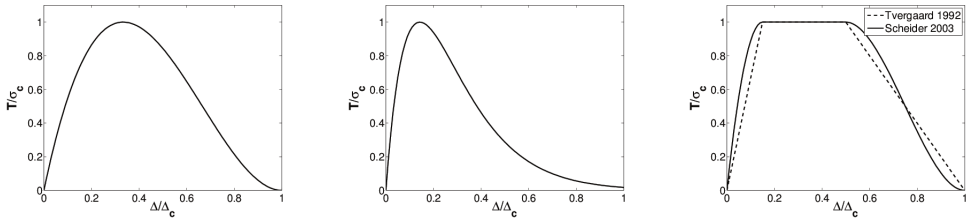

(a) Polynomial [4]. (b) Exponential [5]. (c) Trapezoidal [6, 7].

Figure 1. Different (intrinsic) cohesive laws.

spherical inclusion in a ductile matrix, A. Needleman [4] suggested to have recourse to a polynomial potential law, as depicted on Figure 1(a). Even if this shape is not based on experimental evidences, it allows obtaining a path independent law which models only a normal opening. This limitation was removed by an extension of the polynomial potential cohesive model supplied by V. Tvergaard [8]. In fact the initial model of A. Needleman was inefficient in case of a mixed mode with a high normal compression as it leads to a negative normal opening. Therefore, V. Tvergaard suggested considering a uni-dimensional effective opening to model the mixed mode fracture. Then as the experiments show a universal exponential shape between the binding energy and the atomistic separation, A. Needleman [5, 9] adapted his model and suggested using the exponential cohesive law depicted on Figure 1(b). Nevertheless, this exponential potential law is suitable for brittle materials only and cannot model the dependency of fracture toughness with the plasticity. Toward this end, V. Tvergaard *et al.* developed a trapezoidal cohesive law, first restricted to mode I [6], see Figure 1(c), and then extended to the mixed mode fracture [10]. The dwell region introduced in this law is supposed to model the plastic work of the fracture process. In their study they varied the length of the plateau and demonstrated the little effect of the shape of the cohesive law on the results, except for the initial slope, which influence is discussed below. I. Scheider *et al.* [7] modified this law by inserting quadratic and cubic functions in place of linear branches to remove the slope discontinuity at the extremities of the dwell region, see Figure 1(c). With this modified model they successfully simulated the cup cone fracture of a uni-axial tension test in a 2-D axisymmetric setting. However, the nature of ductile fracture cannot be modeled by this cohesive law. Indeed, ductile fracture involves nucleation, growth and coalescence of micro-cavities which cannot be resolved by a cohesive law with constant fracture parameters. To solve this issue V. Tvergaard *et al.* modified their model and consider a σ_c depending on the plastic strain rate [11].

The different cohesive laws presented above are intrinsic cohesive laws as they model the continuum part of the deformation thanks to an initial slope. This allows inserting cohesive elements, to integrate the TSL, between bulk elements at the very beginning of the simulation, as it was proposed by A. Hillerborg *et al.* [1]. Nevertheless, this slope has to be infinite to obtain a mathematically consistent method [12]. As in practice the slope is finite, the recourse to an intrinsic cohesive law leads to numerical issues as mesh dependency, lift-off and artificial compliance (see [13] for a complete discussion about these issues). To avoid these issues, the development of extrinsic cohesive laws, which can be seen as intrinsic TSLs with an initial infinite slope,

DOI: 10.1002/nme

was pioneered by M. Ortiz *et al.* [14, 15, 16]. When relying on extrinsic TSL, the simulation is initialized with a continuum mesh, and, at onset of fracture, a cohesive element has to be inserted in between two bulk elements. The main drawback of the extrinsic cohesive approach is it complex implementation (especially in a parallel algorithm) as the topology of the mesh has to be modified on the fly during the computation in order to insert the cohesive elements.

The specific case of using a TSL with thin structures was first addressed in the literature by F. Cirak *et al.* [17, 18]. Although they performed the simulations with a shell formulation, they conserved the 3D TSL approach. Therefore to propagate the crack through the thickness they suggested using the Simpson points of the thickness integration.

Among the strategies suggested in the literature to avoid the difficulties inherent to extrinsic and intrinsic approaches, the recourse to a discontinuous Galerkin (DG) formulation seems promising, see [19] for a review. Discontinuous Galerkin methods are now commonly used to solve hyperbolic equations (see [20, 21] for a review) as well as elliptic problems ([22, 23, 24, 25, 26, 27, 28, 29, 30, 31, 32, 33, 34, 35] among others). The main feature of these methods is their ability to take into account discontinuities of the unknown field in the interior domain of studied problems. In such weak formulations the integration by parts is realized on the elements, leading to boundary integral terms ensuring the continuity and compatibility of the solution in a stable and consistent manner. Furthermore the method can be advantageously applied to thin body equations, which require C^1 continuity, to obtain a one-field (displacement) formulation. In this C^0/DG formulation, the C^0 continuity is ensured as usual by considering continuous shape functions and the C^1 continuity is weakly ensured, by DG interface terms, in a stable and consistent way [23, 29, 33, 34, 36, 37, 38]. Recently, with a view toward the combination of DG methods and ECL for thin bodies, the authors [19, 39] have suggested a full-DG formulation of linear beams and shells. In this formulation, the shape functions are discontinuous, and both C^0 and C^1 continuities are weakly ensured by having recourse to the interface terms.

One of the advantages of considering an initially discontinuous mesh when solving mechanical problems, lies in the easiness and efficiency of combining the method with extrinsic cohesive laws. Indeed, as interfaces elements are inserted since the very beginning of the simulation to integrate the interface terms inherent to the DG formulation, an extrinsic cohesive law can be integrated at the onset of fracture by the same interface elements without requiring mesh topology modifications. This technique was pioneered with success for 2D problems by J. Mergheim [40] *et al.* and by Prechtel *et al.* [41], and for 3D problems by R. Radovitzky *et al.* [13, 42]. In particular, in these last references it was demonstrated that this DG/ECL combination has two main advantages. On the one hand the method remains consistent and stress waves are accurately propagated in the structures before a fracture happens, and on the other hand, the parallel implementation of a scalable DG/ECL framework requires little additional efforts compared to the parallel implementation of a traditional continuous FE code. This last advantage results from the absence of dynamic mesh modifications during the simulation process.

As the recourse to 3D elements to model a thin structure leads to a huge number of degrees of freedom, the authors have extended this DG/ECL framework to thin body formulations, first to linear beams [39] and then to linear shells [19]. Toward this end, full-DG formulations of linear beams and shells were developed, where both C^0 and C^1 continuities were ensured by having recourse to the interface terms. However, when considering thin bodies, the implicit representation of the thickness

DOI: 10.1002/nme

implies that the stress field is represented by membrane and bending resultant stresses. Therefore, the ECL has to be redefined for thin bodies, to become based on these resultant stresses. These developments were written under the linear small strain assumption, limiting the applicability of the method to a reduced number of materials exhibiting no plasticity before the crack initiation or propagation.

To remove this limitation, the authors present herein the extension of their full-DG formulation of shells to large deformations. This formulation is able to account for non linear elasto-plastic material behaviors. Thereafter, this formulation is coupled with an ECL to perform the fracture analysis. As for fracture applications very thin meshes are required to model crack propagations, in order to perform simulations in a reasonable computational time, the algorithm is developed in parallel. Note that as the new full-DG method considers more dofs than the initial one-field C^0/DG formulation of shells, it is not efficient for continuum mechanics except to model discontinuities (*e.g.* fracture) or for parallel computations. Indeed, in this last case, a continuous formulation can be used on each processor and the continuity between the mesh partitions can be ensured by having recourse to DG terms.

Beside the validation of the full-DG formulation for finite plasticity with respect to the literature, the combined DG/ECL framework for non-linear shell is validated considering two different applications: the blast of a pressurized cylinder and the crack propagation in a notched tube under internal pressure wave. In particular, the first benchmark was presented by Larsson *et al.* [43], where they compared the crack speed obtained numerically by their XFEM method to experimental results. Larsson *et al.* consider an elastic material behavior and therefore find a numerical crack speed quicker than experiments even if they adapt the fracture parameters to minimize the difference. As they suggest in their paper, an elasto-plastic model allows obtaining results closer to experimental data, as it is proved herein. Indeed, when introducing an elasto-plastic behavior in the combined DG/ECL method, and using literature fracture energy for aluminum alloy, the crack propagation rate found is close to the experimental one. In the elastic case, although the ECL was modified for the fracture energy to account for plastic dissipation [43], results were not in good agreement with experiments [19].

After a brief summary of continuum mechanics of thin bodies in Section 2, the new full-DG formulation of non-linear Kirchhoff-Love shells is derived in Section 3. In this formulation, an hyperelastic-based elasto-plastic constitutive law based on J_2-flow is considered. The aim of Section 4 is to combine this full-DG formulation to the ECL in order to simulate fracture problems. The implementation of this framework in parallel is detailed in Section 5 where the speed-up is illustrated on two examples. The speed-up is a measure of the efficiency of a parallel scheme as it compares the time of simulations performed with different processors numbers. In theory when the number of processors is multiplied by two, the time of the simulation is divided by two. It is shown that the speed-up is just lower than this theoretical value, which proves the efficiency in parallel computations. Finally the Section 6 presents some applications validating the technique. First the full-DG formulation of elasto-plastic shells is validated against benchmarks coming from the literature. Then it is shown that as the hybrid DG/ECL framework allows considering an elasto-plastic constitutive law in combination with the cohesive model, accurate results compared to the experiments are found for fracture dynamics.

DOI: 10.1002/nme

2. CONTINUUM MECHANICS OF KIRCHHOFF-LOVE SHELLS

Continuum mechanics of thin bodies is summarized in this section. More details can be found in several references, [19, 33, 34, 44, 45, 46, 47, 48, 49, 50] among others. In particular [19, 34] use exactly the same notations as this paper.

2.1. Notations

Hereinafter, a subscript will be used to refer to values expressed in the convected basis, while a superscript will be used to refer to values expressed in the conjugate basis. Roman letters as a subscript or superscript substitute for integers between one and three, while Greek letters substitute for integers one or two.

2.2. Kinematics of shells

The kinematics of a thin body, represented on Figure 2, can be described by considering its mid-surface section as a Cosserat plane $\mathcal{A}$ and a third coordinate, representing the thickness, belonging to the constant interval $[h_{\min};\, h_{\max}]$. In the reference frame $\boldsymbol{E}_I$, this representation is written $\boldsymbol{\xi} = \xi^I \boldsymbol{E}_I \,:\, \mathcal{A} \times [h_{\min};\, h_{\max}] \to \mathbb{R}^3$. Using $\boldsymbol{\varphi}\left(\xi^1, \xi^2\right) : \mathcal{A} \to \mathbb{R}^3$ the mapping of the mid-surface and $\boldsymbol{t} : \mathcal{A} \to \mathrm{S}^2 = \left\{\boldsymbol{t} \in \mathbb{R}^3 |_{\|\boldsymbol{t}\|=1}\right\}$ the director of the mid-surface, with S^2 the unit sphere manifold, a configuration $\mathcal{S}$ of the shell is represented by the manifold of positions $\boldsymbol{x}$, which is obtained by the mapping $\boldsymbol{\Phi} : \mathcal{A} \times [h_{\min};\, h_{\max}] \to \mathcal{S}$,

$$\boldsymbol{x} \;=\; \boldsymbol{\Phi}\left(\xi^I\right) = \boldsymbol{\varphi}\left(\xi^\alpha\right) + \xi^3 \lambda_h \boldsymbol{t}\left(\xi^\alpha\right) , \tag{1}$$

where λ_h is the thickness stretch of the shell. By convention, $\mathcal{S}$ refers to the current configuration of the shell, while the reference configuration $\mathcal{S}_0$ is obtained by the mapping $\boldsymbol{\Phi}_0$.

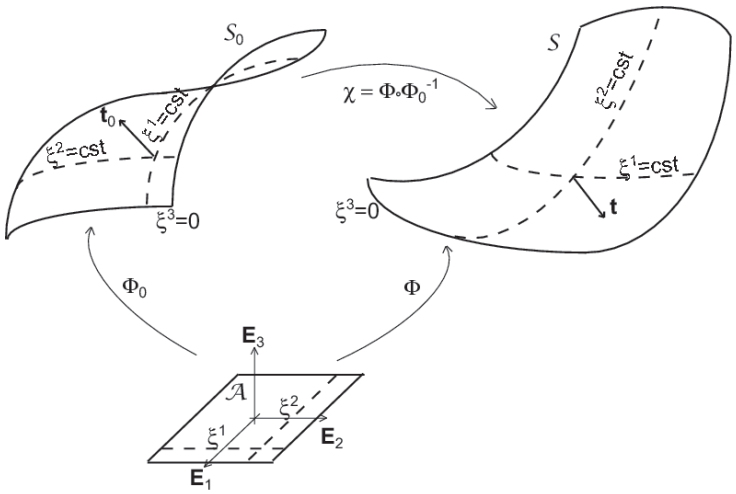

Figure 2. Description of the different configurations of the shell.

Prepared using nmeauth.cls
DOI: 10.1002/nme

Finally, the two-point deformation gradient tensor between these two configurations can be written

$$\mathbf{F} = \boldsymbol{\nabla\Phi} \circ (\boldsymbol{\nabla\Phi}_0)^{-1} = \boldsymbol{g}_i \otimes \boldsymbol{g}_0^i \,, \tag{2}$$

where

$$\boldsymbol{g}_\alpha = \frac{\partial \boldsymbol{\Phi}}{\partial \xi^\alpha} = \boldsymbol{\varphi}_{,\alpha} + \xi^3 \lambda_h \boldsymbol{t}_{,\alpha} + \xi^3 \boldsymbol{t} \lambda_{h,\alpha} \text{ and } \boldsymbol{g}_3 = \frac{\partial \boldsymbol{\Phi}}{\partial \xi^3} = \lambda_h \boldsymbol{t} \,. \tag{3}$$

Practically, the gradient $\lambda_{h,\alpha}$ of the thickness stretch will be neglected in the computation of the deformation gradient.

2.3. *Governing equations of shells*

The governing equations of a thin body are obtained by integrating on the thickness the equations of force and moment equilibrium, leading to

$$\overline{\rho}\ddot{\boldsymbol{\varphi}} - \frac{1}{\bar{j}} \left(\bar{j}\boldsymbol{n}^\alpha\right)_{,\alpha} = 0 \quad \text{on } \mathcal{A}, \text{ and} \tag{4}$$

$$\frac{1}{\bar{j}} \left(\bar{j}\tilde{\boldsymbol{m}}^\alpha\right)_{,\alpha} - \boldsymbol{l} + \lambda \boldsymbol{t} = 0 \quad \text{on } \mathcal{A} \,, \tag{5}$$

where λ is an undefined pressure, $\overline{\rho} = h\rho$ is the density by unit of surface with h the thickness, where $\bar{j} = \det\left(\boldsymbol{\nabla\Phi}\right)_{\xi^3=0}$ is the mapping Jacobian at mid plane, and where the inertia of the director rotation is neglected. Furthermore, the integration on the thickness of the Cauchy stress tensor $\boldsymbol{\sigma}$ leads to the definitions of [44, 45]

$$\boldsymbol{n}^\alpha = \frac{1}{\bar{j}} \int_{h_{\min 0}}^{h_{\max 0}} \boldsymbol{\tau} \boldsymbol{g}^\alpha \det\left(\boldsymbol{\nabla\Phi}_0\right) d\xi^3 \,, \tag{6}$$

$$\boldsymbol{m}^\alpha = \frac{\lambda_h}{\bar{j}} \boldsymbol{t} \wedge \int_{h_{\min 0}}^{h_{\max 0}} \xi^3 \boldsymbol{\tau} \boldsymbol{g}^\alpha \det\left(\boldsymbol{\nabla\Phi}_0\right) d\xi^3 = \lambda_h \boldsymbol{t} \wedge \tilde{\boldsymbol{m}}^\alpha \,, \text{ and} \tag{7}$$

$$\boldsymbol{l} = \frac{1}{\bar{j}} \int_{h_{\min 0}}^{h_{\max 0}} \boldsymbol{\tau} \boldsymbol{g}^3 \det\left(\boldsymbol{\nabla\Phi}_0\right) d\xi^3 \,, \tag{8}$$

respectively the resultant stress vector, the resultant torque vector and the resultant across-the-thickness stress vector written in terms of the Kirchhoff stress tensor $\boldsymbol{\tau} = J\boldsymbol{\sigma}$ ($J = \det\left(\mathbf{F}\right)$ is the deformation gradient Jacobian) for more convenience when expressing the material law. Note that in equations (4) and (5), the external forces are omitted.

In order to define the stress components, the resultant stress vectors are decomposed in the convected basis, as

$$\boldsymbol{n}^\alpha = n^{\alpha\beta}\boldsymbol{\varphi}_{,\beta} + \lambda_h q^\alpha \boldsymbol{t} = \left(\tilde{n}^{\alpha\beta} + \lambda_\mu^\beta \tilde{m}^{\alpha\mu}\right)\boldsymbol{\varphi}_{,\beta} + \lambda_h \left(l^\alpha - \lambda_\mu^\alpha \tilde{m}^{3\mu}\right)\boldsymbol{t} \,, \tag{9}$$

$$\boldsymbol{l} = l^\alpha \boldsymbol{\varphi}_{,\alpha} + l^3 \lambda_h \boldsymbol{t} \,, \text{ and} \tag{10}$$

$$\tilde{\boldsymbol{m}}^\alpha = \tilde{m}^{\alpha\beta}\boldsymbol{\varphi}_{,\beta} + \lambda_h \tilde{m}^{3\alpha}\boldsymbol{t} \,. \tag{11}$$

DOI: 10.1002/nme

In these expressions, $\tilde{n}^{\alpha\beta}$ is the resultant membrane stress, $\tilde{m}^{\alpha\beta}$ is the resultant stress couple, l^{α} is the resultant out-of-plane stress, $\tilde{m}^{\alpha 3}$ is the out-of-plane stress couple and $\lambda_{\mu}^{\beta} = \lambda_h \boldsymbol{t}_{,\mu} \cdot \boldsymbol{\varphi}^{,\beta}$ characterizes the curvature of the shell.

Under Kirchhoff-Love shell assumption, l^{α} can be neglected for isotropic materials, but it is kept temporarily in the equations in order to develop the full-DG formulation. Furthermore, with the same assumption, the normal to the shell can be computed by,

$$\boldsymbol{t} \quad = \quad \frac{\boldsymbol{\varphi}_{,1} \wedge \boldsymbol{\varphi}_{,2}}{||\boldsymbol{\varphi}_{,1} \wedge \boldsymbol{\varphi}_{,2}||} \,, \tag{12}$$

and one directly has $\bar{j} = \lambda_h \, \|\boldsymbol{\varphi}_{,1} \wedge \boldsymbol{\varphi}_{,2}\|$. This particular way of introducing the Kirchhoff-Love assumption in the kinematics of shells was previously suggested by F. Cirak *et al.* [49, 50].

This set of governing equations is accompanied by conventional boundary conditions applied on the boundary $\partial\mathcal{A}$ of the mid-surface $\mathcal{A}$ (see [34] for details).

2.4. *Constitutive laws*

The resolution of the set of equations (4 - 5) requires a constitutive law linking the deformations to the stresses. Herein, depending on the application, an extended compressible neo-Hookean or a J_2-flow elasto-plastic constitutive behavior is considered.

2.4.1. Extended compressible neo-Hookean constitutive law The extended compressible neo-Hookean constitutive model is an hyperelastic law considering an elastic response with the potential,

$$W \quad = \quad \left(\frac{K_0}{2} - \frac{G_0}{3} \right) \log^2 J - G_0 \log J + \frac{G_0}{2} \left(\mathrm{tr}\mathbf{C} - 3 \right) \,, \tag{13}$$

where K_0 and G_0 are respectively the bulk and the shear Moduli of the material and where $\mathbf{C}$ is the right-Cauchy strain tensor computed from

$$\mathbf{C} = \quad \mathbf{F}^T\mathbf{F} \quad = \boldsymbol{g}_i \cdot \boldsymbol{g}_j \boldsymbol{g}_0^i \otimes \boldsymbol{g}_0^j \,, \tag{14}$$

as suggested by F. Cirak *et al.* [50].

2.4.2. J_2-flow elasto-plastic constitutive law In the J_2-flow elasto-plastic model, the plastic behavior is taken into account by the J_2-flow theory with an isotropic linear hardening. The model is based on hyperelastic formulation, which implies the assumption of a multiplicative decomposition of the deformation gradient $\mathbf{F}$ into an elastic part $\mathbf{F}^e$ and a plastic part $\mathbf{F}^p$. The stress tensor derives from a bi-logarithmic potential W,

$$W\left(\mathbf{C}^e\right) \quad = \quad \frac{K_0}{2} \log J^2 + \frac{G_0}{4} \left[\log \mathbf{C}^e\right]^{\mathrm{dev}} : \left[\log \mathbf{C}^e\right]^{\mathrm{dev}} \tag{15}$$

with K_0 and G_0 respectively the bulk and the shear Moduli of the material. As W should only depends on the elastic deformation, the elastic right-Cauchy strain tensor, defined by $\mathbf{C}^e = \mathbf{F}^{eT}\mathbf{F}^e$,

DOI: 10.1002/nme

is considered in (15). Using these definitions the first Piola-Kirchhoff stress tensor can be written

$$\mathbf{P} \quad = \quad 2\mathbf{F} \cdot \left[(\mathbf{F}^p)^{-1} \frac{\partial W(\mathbf{C}^e)}{\partial \mathbf{C}^e} (\mathbf{F}^p)^{-T} \right] . \tag{16}$$

Then, the incremental theory can be used to determine the stresses at stage $n+1$ from the known values at stage n as it is described in [51, 52].

2.4.3. Thickness integration Finally, the determination of thickness stretch (λ_h) has to be specified. The thickness is discretized with 11 integration points following a Simpson integration rule. Then, the local λ_h^p stretch is determined at each point using Newton-Raphson iterations satisfying locally the plane stress requirement $\tau^{33} = 0$. Toward this end, the Kirchhoff stress tensor $\boldsymbol{\tau} = \mathbf{P}\mathbf{F}^T$ is formulated in the convected basis by

$$\tau^{ij} = \tau_{ij} \boldsymbol{g}^i \otimes \boldsymbol{g}^j . \tag{17}$$

The global thickness stretch λ_h is then determined by the Simpson integration on the 11 local values λ_h^p.

3. FULL-DISCONTINUOUS GALERKIN FORMULATION

In this section, a framework defining a numerical approximation of the shell equations described above, and based on a discontinuous polynomial approximation of the unknown field $\boldsymbol{\varphi}$, is suggested. In this formulation, the resulting discontinuities in the surface mapping $\boldsymbol{\varphi}$ and in the surface director $\boldsymbol{t}$ are taken into account by a new full-discontinuous Galerkin formulation. Note that, as in the previous section, the boundary conditions are intentionally omitted in the developments as it just follows [34]. Furthermore, in order to present the developments in a way as clear as possible, the following common notation is used,

$$(\boldsymbol{b},\ \boldsymbol{c})_a = \int_a \boldsymbol{b} \cdot \boldsymbol{c}\, da . \tag{18}$$

3.1. Weak formulation

At this point, the mid-surface $\mathcal{A}$ is approximated by a discretization $\mathcal{A}_h$ into finite-elements $\mathcal{A}_e$ and instead of seeking the exact solution $\boldsymbol{\varphi}$, a polynomial approximation $\boldsymbol{\varphi}_h$ constitutes the solution to the finite element problem. In this work, a discontinuous polynomial approximation is considered, leading to a discretization with discontinuous elements. Therefore the continuity of the solution has to be weakly ensured.

The purpose of this section is to establish a weak form of the problem stated by the set of equations (4-5) for an approximation $\boldsymbol{\varphi}_h$. Multiplying equation (4) by a test function $\delta\boldsymbol{\varphi}$ and equation (5) by the corresponding variation of unit vector $\lambda_h \delta \boldsymbol{t} = \lambda_h \boldsymbol{t}(\delta\boldsymbol{\varphi})$ states the problem as finding $\boldsymbol{\varphi}_h$ such

DOI: 10.1002/nme

that

$$\sum_e \left(\bar{\rho}\ddot{\boldsymbol{\varphi}}_h,\ \delta\boldsymbol{\varphi}\right)_{\mathcal{A}_e} = \sum_e \left(\left(\bar{j}\boldsymbol{n}^\alpha\left(\boldsymbol{\varphi}_h\right)\right)_{,\alpha},\ \delta\boldsymbol{\varphi}\right)_{\mathcal{A}_e} + \sum_e \left(\left(\bar{j}\tilde{\boldsymbol{m}}^\alpha\left(\boldsymbol{\varphi}_h\right)\right)_{,\alpha} - \bar{j}\boldsymbol{l},\ \delta\boldsymbol{t}\lambda_h\right)_{\mathcal{A}_e}. \tag{19}$$

Integrating by parts these integrals and applying the Gauss theorem lead to

$$\begin{aligned}\sum_e a_d^e(\boldsymbol{\varphi}_h,\delta\boldsymbol{\varphi}) = &-\sum_e a_n^e(\boldsymbol{\varphi}_h,\delta\boldsymbol{\varphi}) + \sum_e \left(\bar{j}\boldsymbol{n}^\alpha\left(\boldsymbol{\varphi}_h\right),\ \delta\boldsymbol{\varphi}\nu_\alpha\right)_{\partial\mathcal{A}_e} - \\ &\sum_e a_m^e(\boldsymbol{\varphi}_h,\delta\boldsymbol{\varphi}) + \sum_e \left(\bar{j}\tilde{\boldsymbol{m}}^\alpha\left(\boldsymbol{\varphi}_h\right),\ \delta\boldsymbol{t}\lambda_h\nu_\alpha\right)_{\partial\mathcal{A}_e} + \\ &\sum_e a_s^e(\boldsymbol{\varphi}_h,\delta\boldsymbol{\varphi}) - \sum_e \left(\bar{j}\boldsymbol{l},\ \int_\alpha \delta\boldsymbol{t}\lambda_h d\alpha'\nu_\alpha\right)_{\partial\mathcal{A}_e}\end{aligned} \tag{20}$$

with the outward unit normal of an element $\boldsymbol{\nu}$, and with the following forms,

$$a_d^e(\boldsymbol{\varphi}_h,\delta\boldsymbol{\varphi}) = \left(\bar{\rho}\ddot{\boldsymbol{\varphi}}_h,\ \delta\boldsymbol{\varphi}\right)_{\mathcal{A}_e}, \tag{21}$$

$$a_n^e(\boldsymbol{\varphi}_h,\delta\boldsymbol{\varphi}) = \left(\bar{j}\boldsymbol{n}^\alpha\left(\boldsymbol{\varphi}_h\right),\ \delta\boldsymbol{\varphi}_{,\alpha}\right)_{\mathcal{A}_e}, \tag{22}$$

$$a_m^e(\boldsymbol{\varphi}_h,\delta\boldsymbol{\varphi}) = \left(\bar{j}\tilde{\boldsymbol{m}}^\alpha\left(\boldsymbol{\varphi}_h\right),\ \left(\delta\boldsymbol{t}\lambda_h\right)_{,\alpha}\right)_{\mathcal{A}_e}, \text{and} \tag{23}$$

$$a_s^e(\boldsymbol{\varphi}_h,\delta\boldsymbol{\varphi}) = \left(\left(\bar{j}\boldsymbol{l}\right)_{,\alpha},\ \int_\alpha \delta\boldsymbol{t}\lambda_h d\alpha'\right)_{\mathcal{A}_e}. \tag{24}$$

In these equations, test functions are chosen as $\lambda_h\delta\boldsymbol{t}$, while the variations of $\boldsymbol{t}\delta\lambda_h$ have been omitted. Indeed, although this variation could lead to a missing equation, in this paper, this equation is substituted by the enforcement of the plane-stress assumption while solving the constitutive model, see Section 2.4. The variation $\delta\lambda_h$ will therefore be omitted in the remaining parts of this work. Notice the unusual integration by parts on the resultant out-of plane stresses performed on $\delta\boldsymbol{t}\lambda_h$ in place of $\left(\bar{j}\boldsymbol{l}\right)_{,\alpha}$ to weakly ensure the out-of plane continuity at the interfaces.

As continuity is not ensured across the internal boundary, the jump $[\![\bullet]\!]$ and mean $\langle\bullet\rangle$ operators are defined, as

$$[\![\bullet]\!] = \bullet^+ - \bullet^-, \text{ and } \langle\bullet\rangle = \frac{1}{2}\left(\bullet^+ + \bullet^-\right). \tag{25}$$

In these relations the bullets represent generic vector fields with

$$\bullet^\pm = \lim_{\varepsilon\to 0^+} \bullet\left(\xi^1 \pm \varepsilon\nu^1, \xi^2 \pm \varepsilon\nu^2\right). \tag{26}$$

If definition (25) of the jump operator is not independent of the choice of the $+$ and $-$ sides of an element edge, when this jump is used in combination with the outward unit normal of the $-$ element $\boldsymbol{\nu}^-$, the formulation becomes consistent and independent on this choice.

DOI: 10.1002/nme

From these definitions, the boundary terms of equation (20) read

$$\sum_e \left(\bar{j}\boldsymbol{n}^\alpha,\ \delta\boldsymbol{\varphi}\nu_\alpha\right)_{\partial\mathcal{A}_e} = \left(\bar{j}\boldsymbol{n}^\alpha,\ \delta\boldsymbol{\varphi}\nu_\alpha\right)_{\partial\mathcal{A}_h} - \left[\!\left[\left(\bar{j}\boldsymbol{n}^\alpha,\ \delta\boldsymbol{\varphi}\nu_\alpha^-\right)_{\partial_I\mathcal{A}_h}\right]\!\right], \tag{27}$$

$$\sum_e \left(\bar{j}\tilde{\boldsymbol{m}}^\alpha,\ \delta\boldsymbol{t}\lambda_h\nu_\alpha\right)_{\partial\mathcal{A}_e} = \left(\bar{j}\tilde{\boldsymbol{m}}^\alpha,\ \delta\boldsymbol{t}\lambda_h\nu_\alpha\right)_{\partial\mathcal{A}_h} - \left[\!\left[\left(\bar{j}\tilde{\boldsymbol{m}}^\alpha,\ \delta\boldsymbol{t}\lambda_h\nu_\alpha^-\right)_{\partial_I\mathcal{A}_h}\right]\!\right], \tag{28}$$

$$\sum_e \left(\bar{j}\boldsymbol{l},\ \int_\alpha \delta\boldsymbol{t}\lambda_h d\alpha'\nu_\alpha\right)_{\partial\mathcal{A}_e} = \left(\bar{j}\boldsymbol{l},\ \int_\alpha \delta\boldsymbol{t}\lambda_h d\alpha'\nu_\alpha\right)_{\partial\mathcal{A}_h} - \left[\!\left[\left(\bar{j}\boldsymbol{l},\ \int_\alpha \delta\boldsymbol{t}\lambda_h d\alpha'\nu_\alpha^-\right)_{\partial_I\mathcal{A}_h}\right]\!\right]. \tag{29}$$

At this stage, the main idea of DG methods, which consists in the substitution of the jumps by consistent numerical fluxes $\boldsymbol{h}(\bullet,\bullet,\bullet)$, can be applied. In this paper, traditional average fluxes are considered,

$$\boldsymbol{h}\left(\left(\bar{j}\boldsymbol{n}^\alpha\right)^+,\left(\bar{j}\boldsymbol{n}^\alpha\right)^-,\nu_\alpha^-\right) = \left\langle\bar{j}\boldsymbol{n}^\alpha\right\rangle\nu_\alpha^-, \tag{30}$$

$$\boldsymbol{h}\left(\left(\bar{j}\tilde{\boldsymbol{m}}^\alpha\right)^+,\left(\bar{j}\tilde{\boldsymbol{m}}^\alpha\right)^-,\nu_\alpha^-\right) = \left\langle\bar{j}\tilde{\boldsymbol{m}}^\alpha\right\rangle\nu_\alpha^-, \text{ and} \tag{31}$$

$$\boldsymbol{h}\left(\left(\bar{j}\boldsymbol{l}\right)^+,\left(\bar{j}\boldsymbol{l}\right)^-,\nu_\alpha^-\right) = \left\langle\bar{j}\boldsymbol{l}\right\rangle\nu_\alpha^-. \tag{32}$$

These ones can be injected in equations (27 - 29) and the weak form (20) becomes,

$$\begin{aligned}\sum_e a_d^e(\boldsymbol{\varphi}_h,\delta\boldsymbol{\varphi}) = &-\sum_e\left(a_n^e(\boldsymbol{\varphi}_h,\delta\boldsymbol{\varphi})+a_m^e(\boldsymbol{\varphi}_h,\delta\boldsymbol{\varphi})-a_s^e(\boldsymbol{\varphi}_h,\delta\boldsymbol{\varphi})\right)-\\ &\sum_s\left(a_{nI1}^s(\boldsymbol{\varphi}_h,\delta\boldsymbol{\varphi})+a_{mI1}^s(\boldsymbol{\varphi}_h,\delta\boldsymbol{\varphi})-a_{sI1}^s(\boldsymbol{\varphi}_h,\delta\boldsymbol{\varphi})\right),\end{aligned} \tag{33}$$

with,

$$a_{nI1}^s(\boldsymbol{\varphi}_h,\delta\boldsymbol{\varphi}) = \left(\left\langle\bar{j}\boldsymbol{n}^\alpha\right\rangle,\ \left[\!\left[\delta\boldsymbol{\varphi}\right]\!\right]\nu_\alpha^-\right)_s, \tag{34}$$

$$a_{mI1}^s(\boldsymbol{\varphi}_h,\delta\boldsymbol{\varphi}) = \left(\left\langle\bar{j}\tilde{\boldsymbol{m}}^\alpha\right\rangle,\ \left[\!\left[\delta\boldsymbol{t}\lambda_h\right]\!\right]\nu_\alpha^-\right)_s, \text{ and} \tag{35}$$

$$a_{sI1}^s(\boldsymbol{\varphi}_h,\delta\boldsymbol{\varphi}) = \left(\left\langle\bar{j}\boldsymbol{l}\right\rangle,\ \left[\!\left[\int_\alpha\delta\boldsymbol{t}\lambda_h d\alpha'\right]\!\right]\nu_\alpha^-\right)_s = 0. \tag{36}$$

The last identity results from the assumption of isotropic plane stress state assumed herein leading to $\boldsymbol{l}\approx 0$.

Equation (33) describes a consistent solution of the problem but as a discontinuous polynomial approximation is considered, the continuity is not ensured, and solution is not unique. The weak continuities (C^0 and C^1) enforcement can be achieved with the same argumentation,

$$\begin{aligned}0 = &\left(\left[\!\left[\boldsymbol{\varphi}\right]\!\right],\ \left\langle\delta\left(\bar{j}\boldsymbol{n}^\alpha\right)\right\rangle\nu_\alpha^-\right)_{\partial_I\mathcal{A}_h}+\left(\left[\!\left[\boldsymbol{t}\left(\boldsymbol{\varphi}_h\right)\right]\!\right],\ \left\langle\delta\left(\bar{j}\lambda_h\tilde{\boldsymbol{m}}^\alpha\right)\right\rangle\nu_\alpha^-\right)_{\partial_I\mathcal{A}_h}-\\ &\left(\left[\!\left[\int_\alpha\lambda_h\boldsymbol{t}d\alpha'\right]\!\right],\ \left\langle\delta\left(\bar{j}\boldsymbol{l}\right)\right\rangle\nu_\alpha^-\right)_{\partial_I\mathcal{A}_h}.\end{aligned} \tag{37}$$

In this last expression, $\delta\left(\bar{j}\boldsymbol{n}^\alpha\right)$, $\delta\left(\bar{j}\lambda_h\tilde{\boldsymbol{m}}^\alpha\right)$ and $\delta\left(\bar{j}\boldsymbol{l}\right)$ have to be defined. As it has been demonstrated in previous works for non-linear solid mechanics [32, 34], these expressions would actually depend on the elastic part of the tangent modulus of the constitutive models. But, since the

DOI: 10.1002/nme

purpose of these terms is to ensure that equation (37) is energetically consistent with (33), other forms of the fluxes can be chosen, as long as the consistency condition remains satisfied. Ideally these terms should, when linearized, lead to a symmetric formulation and to the same expressions as the ones suggested for linear elasticity [19, 33]. This argumentation leads to consider the value given for non-linear elasticity in [34] for $\delta\left(\bar{j}\lambda_h\tilde{\boldsymbol{m}}^\alpha\right)$,

$$\delta\left(\bar{j}\lambda_h\tilde{\boldsymbol{m}}^\alpha\right) = \bar{j}_0\mathcal{H}_m^{\alpha\beta\gamma\delta}\left(\delta\boldsymbol{\varphi}_{,\gamma}\cdot\boldsymbol{t}_{,\delta}+\boldsymbol{\varphi}_{h,\gamma}\cdot\delta\boldsymbol{t}_{,\delta}\right)\boldsymbol{\varphi}_{h,\beta}+\bar{j}\lambda_h\tilde{\boldsymbol{m}}^\alpha\boldsymbol{\varphi}_h^{,\beta}\delta\boldsymbol{\varphi}_{,\beta}\,, \tag{38}$$

with the linearized bending stiffness,

$$\begin{aligned}\mathcal{H}_m^{\alpha\beta\gamma\delta} = \frac{E\left(h_{\max}-h_{\min}\right)^3}{12\left(1-\nu^2\right)}\Big[&\nu\boldsymbol{\varphi}_0^{,\alpha}\cdot\boldsymbol{\varphi}_0^{,\beta}\;\;\boldsymbol{\varphi}_0^{,\gamma}\cdot\boldsymbol{\varphi}_0^{,\delta}+\frac{1}{2}\left(1-\nu\right)\boldsymbol{\varphi}_0^{,\alpha}\cdot\boldsymbol{\varphi}_0^{,\gamma}\;\;\boldsymbol{\varphi}_0^{,\delta}\cdot\boldsymbol{\varphi}_0^{,\beta}+\\&\frac{1}{2}\left(1-\nu\right)\boldsymbol{\varphi}_0^{,\alpha}\cdot\boldsymbol{\varphi}_0^{,\delta}\;\;\boldsymbol{\varphi}_0^{,\gamma}\cdot\boldsymbol{\varphi}_0^{,\beta}\Big]\,.\end{aligned} \tag{39}$$

The same principle can be applied to $\delta\left(\bar{j}\lambda_h\boldsymbol{n}^\alpha\right)$ (see Annexe A for details), leading to

$$\begin{aligned}\delta\left(\bar{j}\boldsymbol{n}^\alpha\right) = &\frac{\bar{j}_0}{2}\mathcal{H}_n^{\alpha\beta\gamma\delta}\left(\delta\boldsymbol{\varphi}_{,\gamma}\cdot\boldsymbol{\varphi}_{h,\delta}+\boldsymbol{\varphi}_{h,\gamma}\cdot\delta\boldsymbol{\varphi}_{,\delta}\right)\boldsymbol{\varphi}_{h,\beta}+\bar{j}\boldsymbol{n}^\alpha\cdot\boldsymbol{\varphi}_h^{,\beta}\delta\boldsymbol{\varphi}_{,\beta}\\+&\frac{\bar{j}_0}{\lambda_h}\lambda_\mu^\beta\mathcal{H}_m^{\alpha\mu\gamma\delta}\left(\delta\boldsymbol{\varphi}_{,\gamma}\cdot\boldsymbol{t}_{,\delta}+\boldsymbol{\varphi}_{h,\gamma}\cdot\delta\boldsymbol{t}_{,\delta}\right)\boldsymbol{\varphi}_{h,\beta}\\+&\bar{j}\lambda_h\tilde{m}^{\alpha\mu}\left(\delta\boldsymbol{t}_{,\mu}\cdot\boldsymbol{\varphi}_h^{,\beta}-\frac{\lambda_\mu^\zeta}{\lambda_h}\boldsymbol{\varphi}_h^{,\beta}\cdot\delta\boldsymbol{\varphi}_{,\zeta}\right)\boldsymbol{\varphi}_{h,\beta}\,,\end{aligned} \tag{40}$$

with $\tilde{m}^{\alpha\mu}=\tilde{\boldsymbol{m}}^\alpha\cdot\boldsymbol{\varphi}_h^{,\mu}$, with $\lambda_\mu^\beta=\lambda_h\boldsymbol{t}_{,\mu}\cdot\boldsymbol{\varphi}_h^{,\beta}$, and with the linearized membrane stiffness,

$$\begin{aligned}\mathcal{H}_n^{\alpha\beta\gamma\delta} = \frac{E\left(h_{\max}-h_{\min}\right)}{1-\nu^2}\Big[&\nu\boldsymbol{\varphi}_0^{,\alpha}\cdot\boldsymbol{\varphi}_0^{,\beta}\;\;\boldsymbol{\varphi}_0^{,\gamma}\cdot\boldsymbol{\varphi}_0^{,\delta}+\frac{1}{2}\left(1-\nu\right)\boldsymbol{\varphi}_0^{,\alpha}\cdot\boldsymbol{\varphi}_0^{,\gamma}\;\;\boldsymbol{\varphi}_0^{,\delta}\cdot\boldsymbol{\varphi}_0^{,\beta}+\\&\frac{1}{2}\left(1-\nu\right)\boldsymbol{\varphi}_0^{,\alpha}\cdot\boldsymbol{\varphi}_0^{,\delta}\;\;\boldsymbol{\varphi}_0^{,\gamma}\cdot\boldsymbol{\varphi}_0^{,\beta}\Big]\,.\end{aligned} \tag{41}$$

Finally, remembering the assumption $\boldsymbol{l}\approx 0$, we can take $\delta\left(\bar{j}\boldsymbol{l}\right)=0$.

Introducing equations (38) and (40) into equation (33) leads to

$$\begin{aligned}\sum_e a_d^e(\boldsymbol{\varphi}_h,\delta\boldsymbol{\varphi}) = &-\sum_e\left(a_n^e(\boldsymbol{\varphi}_h,\delta\boldsymbol{\varphi})+a_m^e(\boldsymbol{\varphi}_h,\delta\boldsymbol{\varphi})-a_s^e(\boldsymbol{\varphi}_h,\delta\boldsymbol{\varphi})\right)-\\&\sum_s\left(a_{nI1}^s(\boldsymbol{\varphi}_h,\delta\boldsymbol{\varphi})+a_{mI1}^s(\boldsymbol{\varphi}_h,\delta\boldsymbol{\varphi})-a_{sI1}^s(\boldsymbol{\varphi}_h,\delta\boldsymbol{\varphi})+\right.\\&\left.a_{nI2}^s(\boldsymbol{\varphi}_h,\delta\boldsymbol{\varphi})+a_{mI2}^s(\boldsymbol{\varphi}_h,\delta\boldsymbol{\varphi})-a_{sI2}^s(\boldsymbol{\varphi}_h,\delta\boldsymbol{\varphi})\right)\,,\end{aligned} \tag{42}$$

with the forms,

$$a_{nI2}^s(\boldsymbol{\varphi}_h,\delta\boldsymbol{\varphi}) = \left(\left[\!\left[\boldsymbol{\varphi}_h\right]\!\right],\,\left\langle\delta\left(\bar{j}\boldsymbol{n}^\alpha\right)\right\rangle\nu_\alpha^-\right)_s\,, \tag{43}$$

$$a_{mI2}^s(\boldsymbol{\varphi}_h,\delta\boldsymbol{\varphi}) = \left(\left[\!\left[\boldsymbol{t}\left(\boldsymbol{\varphi}_h\right)\right]\!\right],\,\left\langle\delta\left(\bar{j}\tilde{\boldsymbol{m}}^\alpha\right)\right\rangle\nu_\alpha^-\right)_s\,,\text{ and} \tag{44}$$

$$a_{sI2}^s(\boldsymbol{\varphi}_h,\delta\boldsymbol{\varphi}) = 0\,. \tag{45}$$

DOI: 10.1002/nme

Although this formulation is consistent - consistency results from the introduction of consistent fluxes -, the stability is not ensured. Indeed, linearization of formulation (42) leads to an expression similar to the one obtained for linear elasticity in [19] but for quadratic terms, which should then be added

$$\begin{aligned} a^s_{nI3}(\boldsymbol{\varphi}_h,\delta\boldsymbol{\varphi}) &= \left(\llbracket\boldsymbol{\varphi}_h\rrbracket\cdot\boldsymbol{\varphi}_{h,\gamma}\nu^-_\delta\left\langle\frac{\beta_2\mathcal{H}^{\alpha\beta\gamma\delta}_n\bar{j}_0}{h^s}\right\rangle\boldsymbol{\varphi}_{h,\beta},\ \llbracket\delta\boldsymbol{\varphi}\rrbracket\nu^-_\alpha\right)_s + \\ &\left(\llbracket\boldsymbol{\varphi}_h\rrbracket\cdot\boldsymbol{\varphi}_{h,\gamma}\nu^-_\delta\left\langle\lambda^\beta_\mu\frac{\beta_2\mathcal{H}^{\alpha\mu\gamma\delta}_m\bar{j}_0}{h^s}\right\rangle\boldsymbol{\varphi}_{h,\beta},\ \llbracket\delta\boldsymbol{t}\rrbracket\nu^-_\alpha\right)_s + \\ &\left(\llbracket\boldsymbol{t}\rrbracket\cdot\boldsymbol{\varphi}_{h,\gamma}\nu^-_\delta\left\langle\lambda^\beta_\mu\frac{\beta_2\mathcal{H}^{\alpha\mu\gamma\delta}_m\bar{j}_0}{h^s}\right\rangle\boldsymbol{\varphi}_{h,\beta},\ \llbracket\delta\boldsymbol{\varphi}\rrbracket\nu^-_\alpha\right)_s, \end{aligned} \tag{46}$$

$$a^s_{mI3}(\boldsymbol{\varphi}_h,\delta\boldsymbol{\varphi}) = \left(\llbracket\boldsymbol{t}\left(\boldsymbol{\varphi}_h\right)\rrbracket\cdot\boldsymbol{\varphi}_{h,\gamma}\nu^-_\delta\left\langle\frac{\beta_1\mathcal{H}^{\alpha\beta\gamma\delta}_m\bar{j}_0}{h^s}\right\rangle\boldsymbol{\varphi}_{h,\beta},\ \llbracket\delta\boldsymbol{t}\left(\boldsymbol{\varphi}_h\right)\rrbracket\nu^-_\alpha\right)_s, \tag{47}$$

$$a^s_{sI3}(\boldsymbol{\varphi}_h,\delta\boldsymbol{\varphi}) = \left(\llbracket\boldsymbol{\varphi}_h\rrbracket\cdot\boldsymbol{t}\left(\boldsymbol{\varphi}_h\right)\nu^-_\beta\left\langle\frac{\beta_3\mathcal{H}^{\alpha\beta}_s\bar{j}_0}{h^s}\right\rangle\boldsymbol{t}\left(\boldsymbol{\varphi}_h\right),\ \llbracket\delta\boldsymbol{\varphi}\rrbracket\nu^-_\alpha\right)_s, \tag{48}$$

with the shearing stiffness,

$$\mathcal{H}^{\alpha\beta}_s = G\left(h_{\max}-h_{\min}\right)\frac{A'}{A}\boldsymbol{\varphi}_0^{,\alpha}\cdot\boldsymbol{\varphi}_0^{,\beta}. \tag{49}$$

In this last expression A'/A characterizes the reduced shear area.

The expressions of two first terms (46), (47) result from (38), (40), see [39] for details. The third one is obtained by considering a quadratic form coming from expression of $a^s_{sI1}(\boldsymbol{\varphi}_h,\delta\boldsymbol{\varphi})$ and $a^s_{sI2}(\boldsymbol{\varphi}_h,\delta\boldsymbol{\varphi})$ without the assumption of an isotropic plane stress state, yielding

$$a^s_{sI3}(\boldsymbol{\varphi}_h,\delta\boldsymbol{\varphi})' = \left(\left\{\left[\!\!\left[\int_\mu\boldsymbol{t}_\gamma\boldsymbol{\varphi}_h^{,\gamma}d\mu'\right]\!\!\right]\cdot\boldsymbol{\varphi}_{h,\alpha}\nu^-_\mu\left\langle\frac{\beta_3\mathcal{H}^{\alpha\beta}_s\bar{j}_0}{h^s}\right\rangle\boldsymbol{\varphi}_{h,\beta},\ \left[\!\!\left[\int_\nu\delta\boldsymbol{t}_\delta\boldsymbol{\varphi}_h^{,\delta}d\nu'\right]\!\!\right]\nu^-_\nu\right\}\right)_s. \tag{50}$$

The presence of a primitive $\int_\mu$ in this expression leads to an implementation issue. As discussed in [19], this one is avoided by having recourse to a planar assumption, leading to equation (48). Note that under this hypothesis the two last terms of $a^s_{nI3}(\boldsymbol{\varphi}_h,\delta\boldsymbol{\varphi})$ (46) can also be neglected.

These three quadratic terms depend on dimensionless stabilization parameters β_i that have to be chosen large enough to stabilize the weak statement of the problem. They are independent of the geometry and material properties.

Therefore, after adding such a contribution, the final weak statement of the problem reads,

$$\begin{aligned} a(\boldsymbol{\varphi}_h,\delta\boldsymbol{\varphi}) &= \sum_e\left(a^e_d(\boldsymbol{\varphi}_h,\delta\boldsymbol{\varphi})+a^e_n(\boldsymbol{\varphi}_h,\delta\boldsymbol{\varphi})+a^e_m(\boldsymbol{\varphi}_h,\delta\boldsymbol{\varphi})\right)+ \\ &\sum_s\left(a^s_{nI}(\boldsymbol{\varphi}_h,\delta\boldsymbol{\varphi})+a^s_{mI}(\boldsymbol{\varphi}_h,\delta\boldsymbol{\varphi})-a^s_{sI}(\boldsymbol{\varphi}_h,\delta\boldsymbol{\varphi})\right)=0, \end{aligned} \tag{51}$$

with,

$$a^s_{nI}(\boldsymbol{\varphi}_h,\delta\boldsymbol{\varphi}) = a^s_{nI1}(\boldsymbol{\varphi}_h,\delta\boldsymbol{\varphi})+a^s_{nI2}(\boldsymbol{\varphi}_h,\delta\boldsymbol{\varphi})+a^s_{nI3}(\boldsymbol{\varphi}_h,\delta\boldsymbol{\varphi}), \tag{52}$$

$$a^s_{mI}(\boldsymbol{\varphi}_h,\delta\boldsymbol{\varphi}) = a^s_{mI1}(\boldsymbol{\varphi}_h,\delta\boldsymbol{\varphi})+a^s_{mI2}(\boldsymbol{\varphi}_h,\delta\boldsymbol{\varphi})+a^s_{mI3}(\boldsymbol{\varphi}_h,\delta\boldsymbol{\varphi})\ \text{ and,} \tag{53}$$

$$a^s_{sI}(\boldsymbol{\varphi}_h,\delta\boldsymbol{\varphi}) = a^s_{sI3}(\boldsymbol{\varphi}_h,\delta\boldsymbol{\varphi}). \tag{54}$$

DOI: 10.1002/nme

Furthermore, if continuous test and trial functions are used, $[\![\boldsymbol{\varphi}_h]\!] = [\![\delta\boldsymbol{\varphi}]\!] = 0$ and for a quasi-static problem (*i.e.* $a_d^e(\boldsymbol{\varphi}_h, \delta\boldsymbol{\varphi}) = 0$), equation (51) simplifies into

$$a(\boldsymbol{\varphi}_h, \delta\boldsymbol{\varphi}) \quad = \quad \sum_e a_n^e(\boldsymbol{\varphi}_h, \delta\boldsymbol{\varphi}) + \sum_e a_m^e(\boldsymbol{\varphi}_h, \delta\boldsymbol{\varphi}) + \sum_s a_{mI}^s(\boldsymbol{\varphi}_h, \delta\boldsymbol{\varphi}) = 0\,, \tag{55}$$

which is identical to the non-linear C^0/DG formulation presented in [34].

The final resulting form $a(\boldsymbol{\varphi}_h, \delta\boldsymbol{\varphi})$ (51) of the problem contains the classical terms of shell theory $a_n^e(\boldsymbol{\varphi}_h, \delta\boldsymbol{\varphi})$ and $a_m^e(\boldsymbol{\varphi}_h, \delta\boldsymbol{\varphi})$, while the third term is a collection of boundary integrals resulting from the inter-element discontinuities. They enforce respectively

(i) the consistency of the formulation for $a_{nI1}^s(\boldsymbol{\varphi}_h, \delta\boldsymbol{\varphi})$ and $a_{mI1}^s(\boldsymbol{\varphi}_h, \delta\boldsymbol{\varphi})$,
(ii) the symmetric nature of the Jacobian for $a_{nI2}^s(\boldsymbol{\varphi}_h, \delta\boldsymbol{\varphi})$ and $a_{mI2}^s(\boldsymbol{\varphi}_h, \delta\boldsymbol{\varphi})$, and
(iii) the stability for $a_{nI3}^s(\boldsymbol{\varphi}_h, \delta\boldsymbol{\varphi})$, $a_{mI3}^s(\boldsymbol{\varphi}_h, \delta\boldsymbol{\varphi})$ and $a_{sI}^s(\boldsymbol{\varphi}_h, \delta\boldsymbol{\varphi})$.

3.2. Numerical properties

This section studies the fundamental numerical properties of a numerical methods: consistency, stability and convergence. The first one is obvious since equation (51) is based on consistent numerical fluxes.

Furthermore, as it is lengthy discussed in [34], the stability and convergence can only be demonstrated after linearization of the equations. Therefore, as the linearization of equation (51) leads to the linear full-DG formulation presented in [19], the method inherits in the linear range from its properties. Thus, stability is ensured if the parameters β_1 and β_2 are large enough, if β_3 is non-zero, and with the use of the approximation (48). As it is lengthy discussed in [39] for linear beams, in order to reduce locking and to preserve stability, the optimal value for β_3 is $\beta_1 \left(\frac{h}{L_c}\right)^2$, where h is the thickness of shell and L_c is a characteristic length depending on the problem. Furthermore, the numerical study on the sensitivity of results to the stability parameters was previously presented in the linear range by the authors [19] who concluded, on the one hand that the method is unstable if β_1 and β_2 are lower than 10, and on the other hand, that numerical locking occurs if these parameters are equal or larger than 10 000. But, in a wide range of values $[10\,;\,1000]$ the solution is rather insensitive to the stabilization parameters.

The convergence rate of the method in the energy norm with respect to the mesh size is proved to be equal to $k-1$, with k the degree of the polynomial approximation. Finally, the method presents an optimal-convergence rate $k+1$ in the L^2-norm, which can be demonstrated for at least cubic elements.

4. FRACTURE MECHANICS

The main advantage of a discontinuous Galerkin formulation is obviously its use in fracture mechanic applications. Indeed the presented framework can be coupled with an extrinsic cohesive law in a suitable way as it does not require a topological mesh modification to propagate a crack.

The recourse to a cohesive law for a thin bodies formulation leads to an extra issue compared to a 3D model. Indeed, modeling the through-the-thickness crack propagation is complexified as, on the

DOI: 10.1002/nme

one hand, by the implicit model of the thickness, and on the other hand, by the different behaviors in traction and compression for a crack propagation. Different solutions are suggested in the literature. The simplest one, used by several authors [43, 53, 54, 55], is to consider a constant normal opening over the thickness, which leads to assume that the influence of the modes II and III is negligible, which is the case in many practical situations. A more elaborated model, accounting for the opening in rotation and a mixed mode fracture was introduced by F. Cirak *et al.* [18, 17]. In these references, the authors suggested to use a Simpson integration rule on the thickness to integrate the equations. The recourse to a Simpson integration rule allows evaluating the fracture criterion at different points over the thickness. Therefore F. Cirak *et al.* used the cohesive law only on the Simpson points that met this fracture criterion, allowing propagating the crack through-the-thickness with a distinction between the behaviors in traction and compression. Nevertheless, such an approach requires to move the neutral axis during the crack propagation (otherwise, for a pure bending loading, the crack can only propagate until the initial position of the neutral axis). As moving the neutral axis leads to a very complex implementation (especially to guarantee the continuity of the neutral axis between the adjacent Gauss points) P. Zavattieri [56, 57] suggested to have recourse to an effective opening determined from the different openings in displacements and rotations computed at neutral axis.

In the cohesive model developed herein, we have recourse to the computation of effective openings following the suggestion of P. Zavattieri. Nevertheless, we define the effective openings to release the correct energy during the crack propagation, whatever the loading conditions. Compared to the cohesive model presented by P. Zavattieri, the proposed method avoids the need of extra material parameters to combine openings in displacements and rotations.

This idea of combining a full-DG method with an extrinsic cohesive law was pioneered by J. Mergheim *et al.* [40] and by R. Radovitzky *et al.* [13, 42] in order to avoid the difficulties inherent to the classical cohesive approaches. The main idea of this method can be summarized by substituting the full-DG weak formulation of shells (51) by,

$$\sum_e a^e_{\text{bulk}}(\boldsymbol{\varphi}_h, \delta\boldsymbol{\varphi}) + \sum_s \left[(1-\alpha_s)\, a^s_{\text{inter}}(\boldsymbol{\varphi}_h, \delta\boldsymbol{\varphi}) + \alpha_s a^s_{\text{cohesive}}(\llbracket\boldsymbol{\varphi}_h\rrbracket, \llbracket\delta\boldsymbol{\varphi}\rrbracket)\right] = 0\,, \tag{56}$$

with,

$$\begin{aligned} a^e_{\text{bulk}}(\boldsymbol{\varphi}_h, \delta\boldsymbol{\varphi}) &= a^e_d(\boldsymbol{\varphi}_h, \delta\boldsymbol{\varphi}) + a^e_n(\boldsymbol{\varphi}_h, \delta\boldsymbol{\varphi}) + a^e_m(\boldsymbol{\varphi}_h, \delta\boldsymbol{\varphi})\,, & (57)\\ a^s_{\text{inter}}(\boldsymbol{\varphi}_h, \delta\boldsymbol{\varphi}) &= a^s_{nI1}(\boldsymbol{\varphi}_h, \delta\boldsymbol{\varphi}) + a^s_{nI2}(\boldsymbol{\varphi}_h, \delta\boldsymbol{\varphi}) + a^s_{nI3}(\boldsymbol{\varphi}_h, \delta\boldsymbol{\varphi}) + \\ &\quad a^s_{mI1}(\boldsymbol{\varphi}_h, \delta\boldsymbol{\varphi}) + a^s_{mI2}(\boldsymbol{\varphi}_h, \delta\boldsymbol{\varphi}) + a^s_{mI3}(\boldsymbol{\varphi}_h, \delta\boldsymbol{\varphi}) - \\ &\quad a^s_{sI3}(\boldsymbol{\varphi}_h, \delta\boldsymbol{\varphi})\,, \text{ and} & (58) \end{aligned}$$

$a^s_{\text{cohesive}}(\llbracket\boldsymbol{\varphi}_h\rrbracket, \llbracket\delta\boldsymbol{\varphi}\rrbracket)$ the bi-non-linear form of the cohesive terms that has to be defined. Furthermore, α_s is a Boolean value, switching from "false" to "true" when a fracture criterion is met. Indeed, before onset of fracture, (56) corresponds to the weak form of the shell problem (51), and thus inherits from its numerical properties of consistency and stability. Upon onset of fracture, the interface terms related to the DG framework are replaced by an extrinsic cohesive law, which has still to be defined. Note that in practice the Boolean α_s is evaluated at each Gauss points of interface elements and therefore all Gauss points of an element are not necessarily fractured.

DOI: 10.1002/nme

As discussed above, when considering the theory of thin structures, it is very difficult to separate the thickness part under tension from the part under compression, during a through-the-thickness crack propagation. So we suggested, with success for Euler-Bernoulli beams [39] or linear Kirchhoff-Love shells [19], to apply the cohesive principle to the resultant stresses $\boldsymbol{n}^{\alpha}$ and $\tilde{\boldsymbol{m}}^{\alpha}$, which appear in thin bodies equations. In order to extend this concept to the non-linear range, an effective opening is defined herein for each fracture mode I and II and the combination of both modes is performed by following the idea suggested by G. Camacho *et al.* [14]. Note that in Kirchhoff-Love theory the out-of-plane shearing is neglected, which implies the impossibility to account for a fracture in mode III.

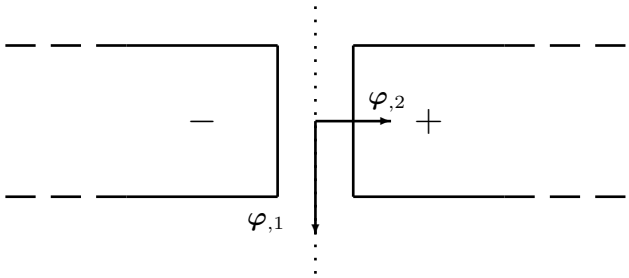

Figure 3. Local basis vectors on the interface element tangential to the shell surface. The interface is drawn with dotted line. By convention, $\boldsymbol{\varphi}_{,1}$ is parallel and $\boldsymbol{\varphi}_{,2}$ is normal to the interface.

Before developing the cohesive law, we assume that the convected basis, tangential to the shell, at the interface element obeys the following rules: vector $\boldsymbol{\varphi}_{,1}$ is parallel to the interface element and $\boldsymbol{\varphi}_{,2}$ is perpendicular to the interface element, as it is illustrated on Figure 3. The computation of the openings in the current basis in place of the reference basis is one of the two main differences with the cohesive model previously presented by the authors for linear Kirchhoff-Love shells [19]. The other one concerns the definition of the effective opening ensuring the appropriate release of energy during crack propagations.

4.1. Mode I

Let us first discuss the case of the mode I opening, illustrated on Figure 4. Considering the convected basis of the interface element shown on Figure 3, the resulting efforts are related to an effective opening whose aim is to consider the two parts (tension and bending) of the normal opening represented on Figure 4.

A normal effective opening, corresponding to the mode I, can be deduced from the tension and bending openings

$$\Delta_n^{\star} \quad = \quad (1-\eta_I)\,\frac{[\![\boldsymbol{\varphi}]\!]^{\star}\cdot\boldsymbol{\varphi}_{,2}}{||\boldsymbol{\varphi}_{,2}||} \pm \eta_I h_I^{\text{eq}}\frac{[\![\boldsymbol{t}]\!]^{\star}\cdot\boldsymbol{\varphi}_{,2}}{||\boldsymbol{\varphi}_{,2}||}\,. \tag{59}$$

In this expression $[\![\boldsymbol{\varphi}]\!]^{\star}$ and $[\![\boldsymbol{t}]\!]^{\star}$ are respectively the effective openings, resulting from the use of a DG method before fracture activation. Indeed at fracture initialization the opening in displacement $[\![\boldsymbol{\varphi}]\!]$ and $[\![\boldsymbol{t}]\!]$ are not exactly equal to zero due to the weak enforcement of compatibility. In order to have null openings at fracture initialization these initial values $[\![\boldsymbol{\varphi}]\!]_0$ and $[\![\boldsymbol{t}]\!]_0$ are subtracted from

DOI: 10.1002/nme

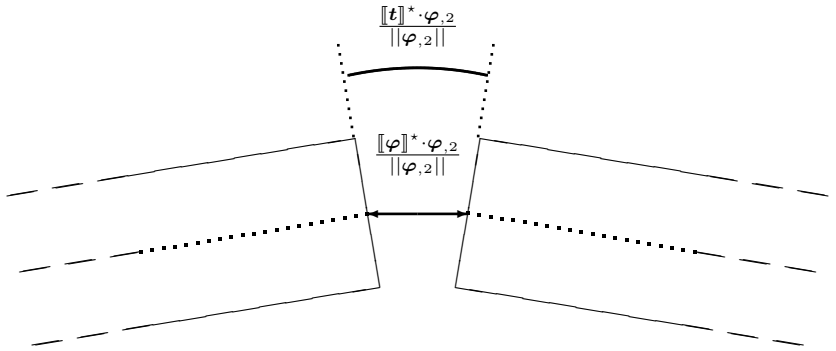

Figure 4. The two components of the normal opening $\Delta_n^\star$, view perpendicular to the shell. The neutral axis is drawn with a dotted line.

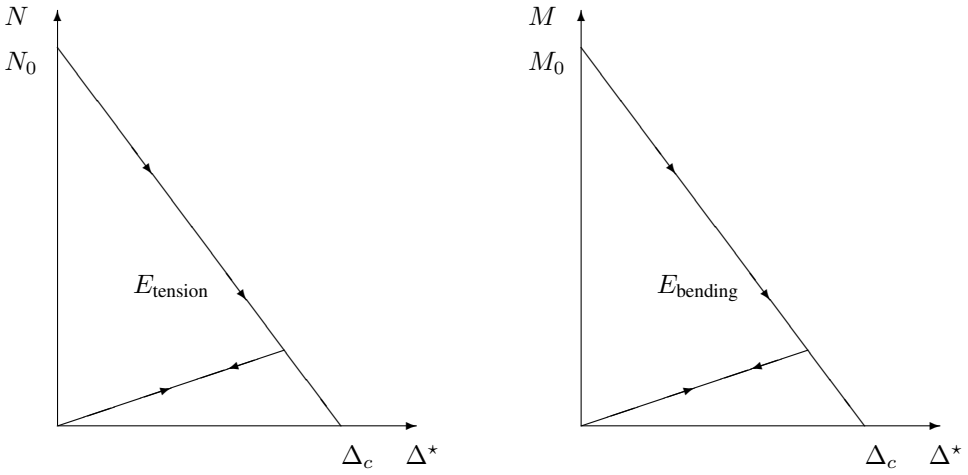

(a) Resultant membrane stress.

(b) Resultant bending stress.

Figure 5. Linearly decreasing monotonic law.

$[\![\boldsymbol{\varphi}]\!]$ and $[\![\boldsymbol{t}]\!]$, yielding

$$[\![\boldsymbol{\varphi}]\!]^\star = [\![\boldsymbol{\varphi}]\!] - [\![\boldsymbol{\varphi}]\!]_0 \,, \tag{60}$$

$$[\![\boldsymbol{t}]\!]^\star = [\![\boldsymbol{t}]\!] - [\![\boldsymbol{t}]\!]_0 \,. \tag{61}$$

Moreover, the parameter η_I ensures that the coupling between the resulting tensile stress and the resulting bending stress respects the energetic balance (*i.e.* that the fracture process releases the correct amount of energy), which is obtained for

$$\eta_I = \frac{\frac{1}{h_I^{\text{eq}}} \left|\tilde{m}_0^{22}\right|}{n_0^{22} + \frac{1}{h_I^{\text{eq}}} \left|\tilde{m}_0^{22}\right|} \,, \tag{62}$$

where n_0^{22} and $\tilde{m}_0^{22}$ are respectively the traction effort and the bending couple at fracture initialization. The factor h_I^{eq} in equations (59) and (62) ensures the respect of the energetic balance,

DOI: 10.1002/nme

as it is demonstrated here below for a pure bending case. Considering the linearly decreasing cohesive law as on Figure 5[†], one has

$$\langle \tilde{m}^{22} \rangle_{\text{coh}} = \tilde{m}_0^{22} \left(1 - \frac{\Delta_n^\star}{\Delta_c} \right) . \tag{63}$$

Assuming that the bending couple leading to fracture corresponds to a critical tensile stress yields

$$\frac{\tilde{m}_0^{22}}{h_I^{\text{eq}}} = h\sigma_{\text{c}} . \tag{64}$$

From this relation, and using the definition of the resulting normal opening (59), the released energy reads

$$\begin{aligned} \int_0^{\Delta_{rc}} \langle \tilde{m}^{22} \rangle_{\text{coh}} \, d \left[\frac{[\![\boldsymbol{t}]\!]^\star \cdot \boldsymbol{\varphi}_{,2}}{||\boldsymbol{\varphi}_{,2}||} \right] &= \int_0^{\Delta_c} \pm \frac{1}{h_I^{\text{eq}}} \langle \tilde{m}_0^{22} \rangle \left(1 - \frac{\Delta_n^\star}{\Delta_c} \right) d\Delta_n^\star \\ &= \frac{1}{h_I^{\text{eq}}} h_I^{\text{eq}} h\sigma_{\text{c}} \frac{\Delta_c}{2} = hG_c , \end{aligned} \tag{65}$$

where $\Delta_{rc} = \frac{[\![\boldsymbol{t}]\!]_c^\star \cdot \boldsymbol{\varphi}_{,2}}{||\boldsymbol{\varphi}_{,2}||} = \frac{1}{h_I^{\text{eq}}} \Delta_c'$ is the critical opening in rotation, for which the fracture process is completed, where G_c and σ_{c} are respectively the fracture energy and a spall stress depending on the material only, where $\Delta_c = \frac{2G_c}{\sigma_{\text{c}}}$ is critical opening for a linear cohesive law (see Figure 5), and where the $\pm$ sign depends on the direction of bending. Let us remark that in relation (59), sign $+$ is used if $\tilde{m}_0^{22} < 0$, while sign $-$ is used otherwise.

Relation (64) provides a relation to compute the value of h_I^{eq}. For a pure bending problem in linear elasticity the fracture at skin occurs for,

$$\tilde{m}_0^{22} = \frac{h^2 \sigma_{\text{c}}}{6} , \tag{66}$$

and thus, using (64) $h_I^{\text{eq}} = \frac{h}{6}$, which corresponds to the value suggested by the authors in the linear range [19].

Nevertheless, in the case of a tension/bending coupled problem, the equivalent thickness has to be computed considering the bending and tensile parts of the stress at fracture onset, leading to

$$\frac{\tilde{m}_0^{22}}{h_I^{\text{eq}}} = h\sigma_{\text{c}} - n_0^{22} . \tag{67}$$

Under the linear elasticity hypothesis, as fracture occurs when $\frac{6\tilde{m}_0^{22}}{h^2} + \frac{n_0^{22}}{h} = \sigma_{\text{c}}$, relation (67) becomes,

$$h_I^{\text{eq}} = \frac{h}{6} , \tag{68}$$

as presented for linear Kirchhoff-Love shells [19].

[†]The demonstration remains valid for another cohesive law.

DOI: 10.1002/nme

4.2. Mode II

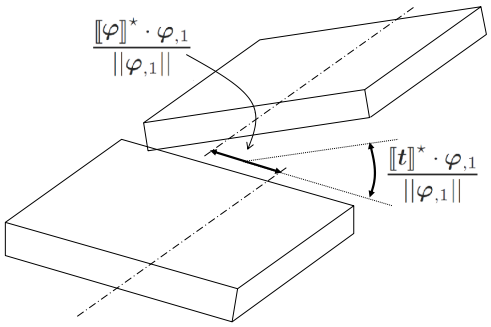

Figure 6. The two components of the tangential opening $\Delta_t^\star$. Before opening, the element axes are the same and the two crack lips are in the same plane.

Following exactly the same lines in mode II, the tangential effective opening drawn on Figure 6 reads,

$$\Delta_t^\star = (1-\eta_{II})\frac{[\![\boldsymbol{\varphi}]\!]^\star \cdot \boldsymbol{\varphi}_{,1}}{||\boldsymbol{\varphi}_{,1}||} \pm \eta_{II} h_{II}^{\text{eq}} \frac{[\![\boldsymbol{t}]\!]^\star \cdot \boldsymbol{\varphi}_{,1}}{||\boldsymbol{\varphi}_{,1}||}\,. \tag{69}$$

In this expression, the parameter η_{II} ensures that the coupling between the resultant shear stress and the resultant torsion respects the energetic balance. This is obtained for

$$\eta_{II} = \frac{\frac{1}{h_{II}^{\text{eq}}}\left|\langle \tilde{m}_0^{21}\rangle\right|}{\langle n_0^{21}\rangle + \frac{1}{h_{II}^{\text{eq}}}\left|\langle \tilde{m}_0^{21}\rangle\right|}\,, \tag{70}$$

where n_0^{21} and $\tilde{m}_0^{21}$ are respectively the shearing effort and the torsion torque at fracture initialization and where the equivalent thickness of mode II ensuring the energetic balance is given by,

$$\frac{\tilde{m}_0^{21}}{h_{II}^{\text{eq}}} = h\tau_c - n_0^{21} = h\beta\sigma_{\text{c}} - n_0^{21}\,, \tag{71}$$

where $\tau_c = \beta\sigma_{\text{c}}$ is the shearing critical strength and where $\beta = \frac{K_{IIc}}{K_{Ic}}$ is the fracture mode coupling parameter. Finally, the sign $+$ is used in equation (69) when $\tilde{m}_0^{21} < 0$, and otherwise the sign $-$ is used, following the same convention given for $\tilde{m}_0^{22}$ in mode I.

4.3. Modes Combination

Now the combination between modes I and II is performed in a similar way as presented by several authors [58, 59, 60, 61, 62, 56, 63] when considering Cauchy stress tensors for 3D TSL. This method, which was first suggested by G. Camacho *et al.* [14], and extended a few years later by M. Ortiz *et al.* [16], considers an effective stress σ_{eff} to detect fracture initialization, with the criterion: $\sigma_{\text{eff}} > \sigma_{\text{c}}$, and allows fracture in compression happening if the shearing stress is sufficiently large,

$$\sigma_{\text{eff}} = \begin{cases} \sqrt{\sigma^2 + \beta^{-2}\tau^2} & \text{if } \sigma \geq 0 \\ \frac{1}{\beta} \ll |\tau| - \mu_c\,|\sigma| \gg & \text{if } \sigma < 0 \end{cases}\,. \tag{72}$$

DOI: 10.1002/nme

In this criterion, σ and τ are respectively the normal and tangential Cauchy stress at the integration point where fracture is evaluated and μ_c is the friction parameter, depending on the material only. The operator $\ll \bullet \gg$ is equal to $\bullet$ if $\bullet \geq 0$, and 0 otherwise. The initiation criterion (72) can still be considered in the present work. Indeed, from the resultant stresses of the shell formulation, the Cauchy stress tensor can be directly evaluated through-the-thickness at each Simpson points.

Furthermore, in the coupled case, the equivalent thickness of modes I and II are determined respectively with the values of $\sigma = \sigma_I$ and $\tau = \tau_{II}$ reached in equation (72) at fracture onset $\sigma_{\text{eff}} = \sigma_{\text{c}}$ leading to,

$$h_I^{\text{eq}} = \frac{\tilde{m}_0^{22}}{h\sigma_I - n_0^{22}} \text{ and,} \tag{73}$$

$$h_{II}^{\text{eq}} = \frac{\tilde{m}_0^{21}}{h\tau_{II} - n_0^{21}}\,. \tag{74}$$

However, in this new formulation of thin structures, the cohesive law should be written in terms of resultant values instead of the Cauchy stress, and some quantities and notations have to be first introduced:

- The effective opening $\Delta^\star$ is a combination of the two effective openings $\Delta_n^\star$ (59) and $\Delta_t^\star$ (69). So $\Delta^\star$ allows taking into account a coupling between the two fracture modes. Its value is an extension of the formulation presented by M. Ortiz *et al.* in [16, 18] to the present cohesive model:

$$\Delta^\star = \sqrt{\ll \Delta_n^\star \gg^2 + \beta^2 \Delta_t^{\star 2}}\,. \tag{75}$$

  The use of the operator $\ll \bullet \gg$ is mandatory. Indeed if the rupture occurs in compression, the normal opening has to be equal to zero, as in compression the normal opening is negative, which means that there is a penetration between elements. Obviously this latter case has no physical meaning and forces have to be introduced between elements. In place of contact forces, the DG terms $a_{nI2}^s(\boldsymbol{\varphi}_h, \delta\boldsymbol{\varphi})$ and $a_{nI3}^s(\boldsymbol{\varphi}_h, \delta\boldsymbol{\varphi})$ (see equations (43) and (46)) can also be used to weakly enforce a zero penetration.
- The critical opening Δ_c is the opening for which the fracture process is completed, meaning no remaining forces exist between the fractured sides. Therefore, for this value, the energy released has to be equal to G_c, and, for linear decreasing monotonic cohesive laws, $\Delta_c = \frac{2G_c}{\sigma_{\text{c}}}$.
- The maximal effective opening reached during the simulation $\Delta_{max}^\star$ is an internal variable tracking the maximum opening history. This one is used to account for an unloading as previously suggested by G. Camacho *et al.* [14].

Now the cohesive law can be formulated in terms of these new definitions. As it is well known that, for brittle materials or materials under the small scale yielding assumption, the shape of the cohesive law has little influence on numerical results, as long as the law is monotonically decreasing, a simple linear decreasing law is considered in this work. In case of unloading the effort decreases linearly to zero (see Figure 5). By application of the cohesive principle on the resultant stress vectors, the new cohesive model reads,

1. Tensile case ($\sigma \geq 0$ at mid-surface),

DOI: 10.1002/nme

- if $\Delta^\star \geq \Delta^\star_{max}$ (loading case),

$$\left\langle \tilde{m}^{22} \right\rangle_{\text{coh}} = \tilde{m}_0^{22} \left(1 - \frac{\Delta^\star}{\Delta_c}\right) \frac{\Delta_n^\star}{\Delta^\star}, \tag{76}$$

$$\left\langle n^{22} \right\rangle_{\text{coh}} = n_0^{22} \left(1 - \frac{\Delta^\star}{\Delta_c}\right) \frac{\Delta_n^\star}{\Delta^\star}, \tag{77}$$

$$\left\langle \tilde{m}^{21} \right\rangle_{\text{coh}} = \tilde{m}_0^{21} \beta \left(1 - \frac{\Delta^\star}{\Delta_c}\right) \frac{|\Delta_t^\star|}{\Delta^\star}, \tag{78}$$

$$\left\langle n^{21} \right\rangle_{\text{coh}} = n_0^{21} \beta \left(1 - \frac{\Delta^\star}{\Delta_c}\right) \frac{|\Delta_t^\star|}{\Delta^\star}, \tag{79}$$

- if $\Delta^\star < \Delta^\star_{max}$ (unloading case),

$$\left\langle \tilde{m}^{22} \right\rangle_{\text{coh}} = \tilde{m}_0^{22} \left(\frac{\Delta^\star}{\Delta^\star_{max}} - \frac{\Delta^\star}{\Delta_c}\right) \frac{\Delta_n^\star}{\Delta^\star}, \tag{80}$$

$$\left\langle n^{22} \right\rangle_{\text{coh}} = n_0^{22} \left(\frac{\Delta^\star}{\Delta^\star_{max}} - \frac{\Delta^\star}{\Delta_c}\right) \frac{\Delta_n^\star}{\Delta^\star}, \tag{81}$$

$$\left\langle \tilde{m}^{21} \right\rangle_{\text{coh}} = \tilde{m}_0^{21} \beta \left(\frac{\Delta^\star}{\Delta^\star_{max}} - \frac{\Delta^\star}{\Delta_c}\right) \frac{|\Delta_t^\star|}{\Delta^\star}, \tag{82}$$

$$\left\langle n^{21} \right\rangle_{\text{coh}} = n_0^{21} \beta \left(\frac{\Delta^\star}{\Delta^\star_{max}} - \frac{\Delta^\star}{\Delta_c}\right) \frac{|\Delta_t^\star|}{\Delta^\star}. \tag{83}$$

2. Compression case ($\sigma < 0$ at mid-surface),

- if $\Delta^\star \geq \Delta^\star_{max}$ (loading case),

$$\left\langle \tilde{m}^{21} \right\rangle_{\text{coh}} = \tilde{m}_0^{21} \left(1 - \frac{\Delta^\star}{\Delta_c}\right), \tag{84}$$

$$\left\langle n^{21} \right\rangle_{\text{coh}} = n_0^{21} \left(1 - \frac{\Delta^\star}{\Delta_c}\right), \tag{85}$$

- if $\Delta^\star < \Delta^\star_{max}$ (unloading case),

$$\left\langle \tilde{m}^{21} \right\rangle_{\text{coh}} = \tilde{m}_0^{21} \left(\frac{\Delta^\star}{\Delta^\star_{max}} - \frac{\Delta^\star}{\Delta_c}\right), \tag{86}$$

$$\left\langle n^{21} \right\rangle_{\text{coh}} = n_0^{21} \left(\frac{\Delta^\star}{\Delta^\star_{max}} - \frac{\Delta^\star}{\Delta_c}\right), \tag{87}$$

where in this last case the condition $\frac{|\Delta_t^\star|}{\Delta^\star} = \frac{1}{\beta}$ (*cf.* equation (75)) is taken into account.

The use of n_0^{22}, $\tilde{m}_0^{22}$, n_0^{21}, $\tilde{m}_0^{21}$ allows guarantying the continuity of stresses at fracture initialization. If this continuity is not ensured, K. Papoulia *et al.* [62] have demonstrated that there are some convergence problems. Furthermore, as at fracture initialization the ratios $\frac{\Delta_n^\star}{\Delta^\star}$ and $\frac{|\Delta_t^\star|}{\Delta^\star}$ are undetermined, their initial values are chosen respectively equal to 1 and $\frac{1}{\beta}$ in order to ensure the stresses continuity at the fracture initiation (*i.e.* the values of reduced stresses and torques have the same values at fracture initiation, no matter they are computed from the bulk material law or cohesive law).

It has to be noticed that the choice of tensile or compressive case is performed at fracture initialization. Therefore, although unloading can be accounted for during the fracture process, as

DOI: 10.1002/nme

shown on Figure 5, this model is not able to shift from a fracture process in tension to a fracture process in compression (*e.g.* start the fracture in compression and end up the fracture in tension). Finally, with these definitions, the cohesive terms $a^s_{\text{cohesive}}(\llbracket\boldsymbol{\varphi}_h\rrbracket, \llbracket\delta\boldsymbol{\varphi}\rrbracket)$ of equation (56) can be written

$$a^s_{\text{cohesive}}(\llbracket\boldsymbol{\varphi}_h\rrbracket, \llbracket\delta\boldsymbol{\varphi}\rrbracket) = \left(\bar{j}\,\langle\boldsymbol{n}^\alpha\rangle_{\text{coh}}\,,\ \llbracket\delta\boldsymbol{\varphi}\rrbracket\,\nu^-_\alpha\right)_s + \left(\bar{j}\,\langle\tilde{\boldsymbol{m}}^\alpha\rangle_{\text{coh}}\,,\ \llbracket\delta\boldsymbol{t}\lambda_h\rrbracket\,\nu^-_\alpha\right)_s\,, \tag{88}$$

where the components of $\langle\boldsymbol{n}^\alpha\rangle_{\text{coh}}$ and $\langle\tilde{\boldsymbol{m}}^\alpha\rangle_{\text{coh}}$ are computed thanks to the set of equations (76 - 87), with other components of the resultant stresses equal to zero. Note that all these definitions depend on the choice of the manifold used on the interface. As mentioned earlier, this paper follows this convention: $\boldsymbol{\varphi}_{,1}$ is parallel to the interface and $\boldsymbol{\varphi}_{,2}$ is perpendicular to the interface, as it is illustrated on Figure 3.

5. PARALLEL IMPLEMENTATION

The full-DG formulation developed in section 3 is implemented in our own finite element code based on Gmsh [64]. Details about the code can be found in [19] and the development of forms (21 - 24, 34 - 35, 43-44, 46-48) are implemented by an extension of the C^0/DG case [34]. To show the versatility of the formulation, quasi-static and dynamic examples are considered and simulations are performed with different kinds of elements:

(i) 6-node quadratic triangles with 3 Gauss points for bulk integration and 3 Gauss points on each edge for interface integration;
(ii) 9-node quadratic quadrilaterals with 4 Gauss points for bulk integration and 3 Gauss points on each edge for interface integration;
(iii) 10-node cubic triangles with 6 Gauss points for bulk integration and 4 Gauss points on each edge for interface integration;
(iv) 16-node quadratic quadrilaterals with 16 Gauss points for bulk integration and 4 Gauss points on each edge for interface integration.

The full-DG framework developed above is pointless when solving continuum mechanics problems as it considers more dofs as the C^0/DG method [34] and therefore leads to an extra computational time. Nevertheless, this formulation can be advantageously used in different situations:

(i) To solve problems which strongly suffer from plasticity-induced locking for low order elements as brought to light by the pinched hemisphere benchmark (see section 6.3).
(ii) To solve fracture mechanic problems, which was discussed in the previous section. However due to the large amount of degrees of freedom involved, a parallel implementation is mandatory.
(iii) To perform parallel computations. In this case, several processors are used in the same time to solve the problem and the mesh is divided between the processors into partitions. Therefore, each processor treats a part of the mesh and the partitions can be linked themselves by having recourse to full-DG method. In this case, the C^0/DG approach is used on each partition and

DOI: 10.1002/nme

the full-DG method is used only at interfaces between partitions to ensure the continuity. As the extra dofs are only inserted between mesh partitions, the extra computational cost is negligible and the method is very scalable.

This section focuses on points (*ii*) and (*iii*) and presents the parallel implementation of a method involving either a C^0/DG or a full-DG discretization in each processor and the use of the full-DG framework at processor interfaces. The method is presented for the explicit Hulbert-Chung time integration algorithm [65] and for 1D interfaces (lines) but can easily be generalized to 2D interfaces for 3D elements. Numerical benchmarks will be performed to prove the scalability of the suggested method (see section 6).

The mesh is divided into partitions by METIS [66], which is used through Gmsh, see Figure 7(a). So each processor owns a partition of the mesh, see Figure 7(b), but also the ghost boundary elements, which are elements of the other processors having a common interface, see Figure 7(c). Thus, using the ghost elements, each processor can create the interface elements in its own partition and at partition interfaces. Finally the interface terms $a^s_{nI1}(\boldsymbol{\varphi}_h, \delta\boldsymbol{\varphi})$, $a^s_{mI1}(\boldsymbol{\varphi}_h, \delta\boldsymbol{\varphi})$, $a^s_{nI2}(\boldsymbol{\varphi}_h, \delta\boldsymbol{\varphi})$, $a^s_{mI2}(\boldsymbol{\varphi}_h, \delta\boldsymbol{\varphi})$, $a^s_{nI3}(\boldsymbol{\varphi}_h, \delta\boldsymbol{\varphi})$, $a^s_{mI3}(\boldsymbol{\varphi}_h, \delta\boldsymbol{\varphi})$, and $a^s_{sI3}(\boldsymbol{\varphi}_h, \delta\boldsymbol{\varphi})$ are integrated on all the interface elements[‡]. As partitions are discontinuous, they do not share common degrees of freedom (dofs),

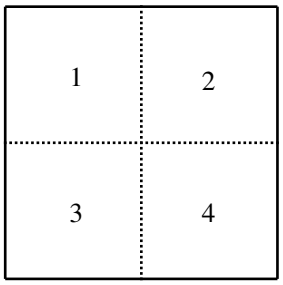

(a) Square plate divided into 4 partitions

1	1	1	1	2	2	2	2
1	1	1	1	2	2	2	2
1	1	1	1	2	2	2	2
1	1	1	1	2	2	2	2
3	3	3	3	4	4	4	4
3	3	3	3	4	4	4	4
3	3	3	3	4	4	4	4
3	3	3	3	4	4	4	4

(b) Meshed plate with partition number for each element

1	1	1	1	2
1	1	1	1	2
1	1	1	1	2
1	1	1	1	2
3	3	3	3	

(c) Mesh partition of processor #1. The ghost elements are in dashed line

Figure 7. Simple mesh partitioning between 4 processors.

and the Gmsh dof manager creates new dofs on each partition, independently on the node numbering (in Gmsh the dof is not directly linked to the node). However, this statement is not true for the ghost elements, which nodal values have to be communicated through the network via MPI when evaluating the interface terms. Also, as interface terms including the ghost elements, are actually computed on two partitions, only the part related to the degrees of freedom really belonging to the partition is assembled in order to avoid duplication. This suggested implementation is more efficient than previously suggested parallel DG formulations [32], as it avoids the communication of values computed from the material law (stress tensors, Hooke tensors ...) when integrating the forces for the interface elements between partitions, and therefore, it leads to a reduced number of communications (only one per time step, communicating the nodal values of ghost elements).

[‡]On interfaces internal to the partition, if the C^0/DG method is used instead of the full-DG method, only $a^s_{mI1}(\boldsymbol{\varphi}_h, \delta\boldsymbol{\varphi})$, $a^s_{mI2}(\boldsymbol{\varphi}_h, \delta\boldsymbol{\varphi})$ and $a^s_{mI3}(\boldsymbol{\varphi}_h, \delta\boldsymbol{\varphi})$ are integrated as the displacement field is continuous from one element to another

DOI: 10.1002/nme

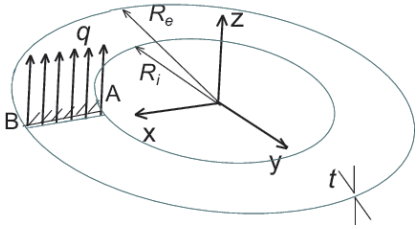

(a) Geometry

Property	Value
Internal Radius	R_i = 6 m
External Radius	R_e = 10 m
Thickness	t = 0.03 m
Young modulus	$E = 2.1\times10^{10}$ N·m^{-2}
Poisson ratio	$\nu = 0$
Applied force	$q = 12000$ N·m^{-1}

(b) Properties

Figure 8. Elastic non-linear plate ring benchmark.

Note that the parallel approach can be generalized to implicit schemes. Indeed to store the structural vectors and matrices, and to perform the associated operations, we rely on the PETSc [67, 68] libraries and on the ghost elements-based approach. For an explicit resolution with the developed ghost elements-based approach, each processor fills the structural vectors as in sequential and the time integration can proceed. For an implicit resolution $\boldsymbol{Ax} = \boldsymbol{b}$, during the assembly process of the elementary terms, each processor has to fill the rows of the structural matrix $\boldsymbol{A}$, and the terms of the structural vectors $\boldsymbol{b}$, corresponding to the bulk degrees of freedom in this processor. The ghost rows of the elementary interface matrices, although computed, are not accounted for during the structural assembly loop. PETSc can then do the reduce and resolution operations in a parallel way. The only limitation is the use of an iterative solver instead of a direct solver.

6. NUMERICAL APPLICATIONS

This section presents some benchmarks to validate the developed full-DG method for non-linear elasto-plastic shells, and to show its ability to solve fracture mechanic problems. Also, results of the C^0/DG formulation (55) and of the full-DG formulation (51) are compared on several examples. Both formulations are one-field formulations based on the displacement field and they have 3 dofs per node. Obviously, the full-DG method has more dofs but it can be advantageously used to solve fracture mechanic problems by combination with a cohesive law, see section 4, or to perform parallel simulations. For all the simulations, the stability parameters are set to $\beta_1 = \beta_2 = \left(\frac{L_c}{h}\right)^2 \beta_3 = 10$, with h the initial shell thickness and L_c, the greatest length of the problem. This choice of a low value for β_1 is motivated by the considerations given in [19, 32, 33, 39], where it is explained that for thin meshes, stable results are obtained for this low value of β_i, and that for explicit time integrations the critical time step, which depends on longitudinal and transverse wave speeds, is also proportional to $\frac{1}{\max\sqrt{\beta_i}}$.

6.1. *Elastic plate ring*

This benchmark was first performed in [69] and consists into a thin plate ring, with an inner radius R_i, an outer radius R_e and a thickness t, with the geometry depicted in Figure 8(a) and the properties reported in Figure 8(b). This ring is cut along a radius AB, and, on one side of this cutting, the plate

Prepared using nmeauth.cls
DOI: 10.1002/nme

is clamped, while a uniform vertical loading q is applied on the other side, see Figure 8(a). This test has widely been used in the literature, see *e.g.* [70, 71, 72, 73] to compare shell formulations when large deformations and rotations arise.

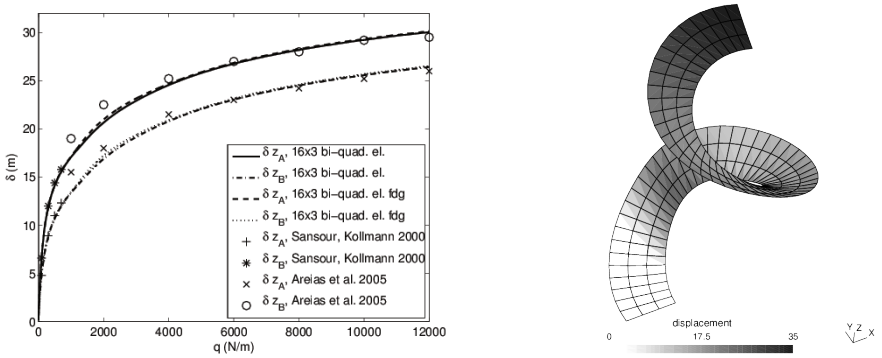

(a) Nodes A & B force *vs.* displacement (b) Final configuration

Figure 9. Elastic non linear plate ring results for C^0/DG and full-DG (fdg) methods.

This simulation is computed using the suggested discontinuous Galerkin formulations (C^0/DG and full-DG) with 8-nodes bi-quadratic elements and an extended compressible neo-Hookean model, see Section 2.4. The final deformed configuration is illustrated in Figure 9(b), and the displacement evolutions of nodes A and B located at the cutting are shown in Figure 9(a). Although the mesh experiences large distortion during the deformation process, the solutions are in good agreement with the ones obtained in the literature, and in particular with:

- The hybrid stress formulation proposed by Sansour and Kollmann [72], from whom results are displayed for q <3000 N·m^{-1} (which is the maximum loading considered in this reference).
- The mixed formulation based on mid-side rotations proposed by Areias *et al.* [73], which converges for an applied linear force reaching 12000 N·m^{-1}.

This proves that the use of the full-DG framework gives results similar to the existing formulations.

6.2. *Simply supported perfectly plastic square plate subjected to uniform loading*

This example studies the central deflection history of the plate depicted on Figure 10(a), which is submitted to a uniform pressure $p_0 = 20.7$ [bars]. Properties of the the elasto-plastic plate are reported in Figure 10(b). This benchmark has first been presented by Belytschko *et al.* [74] and performed again some years later by Swaddiwudhipong *et al.* [75]. The central deflection is computed by the explicit algorithms of Hulbert-Chung [65] without numerical dissipation, for both C^0/DG and full-DG formulations and for successively 8×8 quadratic and cubic quadrilaterals. Results are reported on Figure 11 showing the good correlation with the literature for all the studied elements.

DOI: 10.1002/nme

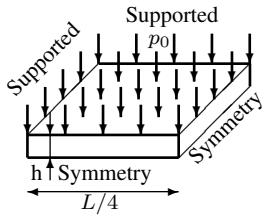

(a) Geometry

Geometry	
Length (L) [mm]	254
Thickness (h) [mm]	12.7
Material	
Density (ρ) [kg/m^3]	2768
Young modulus (E) [MPa]	69000
Poisson ratio (ν) [-]	0.3
Yield stress (σ_y^0) [MPa]	207
Hardening modulus ($\bar{h}$) [MPa]	0

(b) Properties

Figure 10. Simply supported elasto-plastic plate subjected to a uniform loading benchmark.

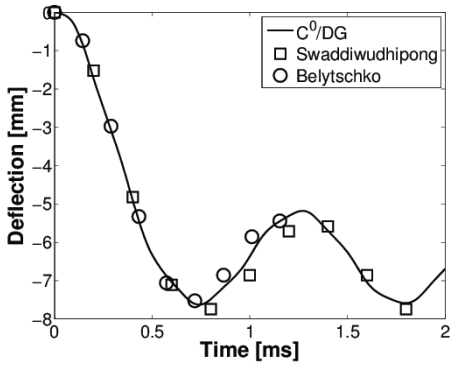

(a) C^0/DG quadratic

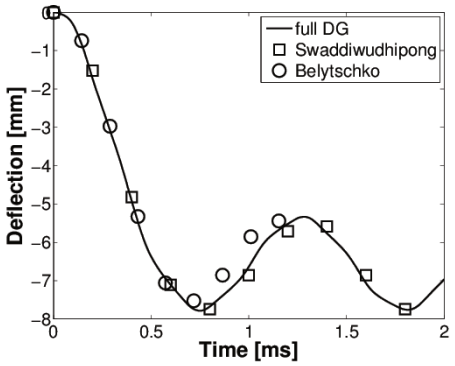

(b) Full DG quadratic

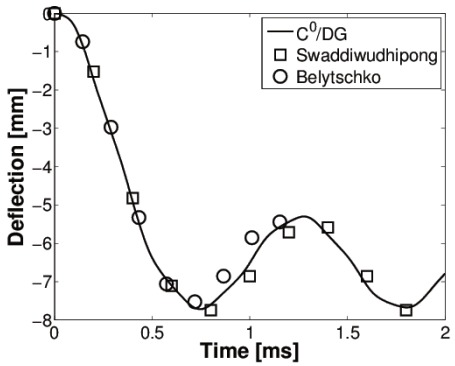

(c) C^0/DG cubic

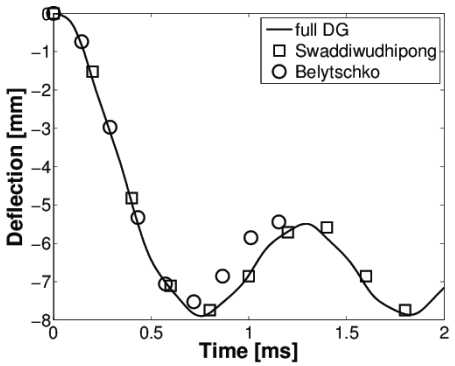

(d) Full DG cubic

Figure 11. Simply supported elasto-plastic plate subjected to a uniform loading results.

6.3. Pinched elasto-plastic hemisphere

The second elasto-plastic benchmark studies the force *vs.* displacement relation of the pinched hemisphere depicted on Figure 12(a), whose material values are reported in Figure 12(b). The hemisphere is loaded on two opposite diameters (one in tension, the other one in compression)

Prepared using nmeauth.cls
DOI: 10.1002/nme

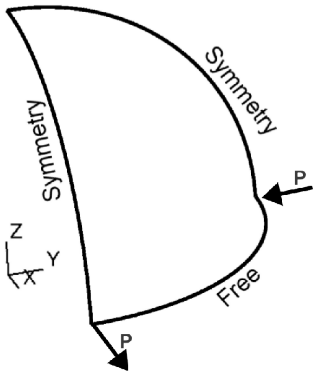

(a) Geometry

Geometry	
Radius (R) [m]	10
Thickness (h) [m]	0.5
Material	
Young modulus (E) [Pa]	10
Poisson ratio (ν) [-]	0.2
Yield stress (σ_y^0) [Pa]	0.2
Hardening modulus ($\overline{h}$) [Pa]	9

(b) Properties

Figure 12. Pinched elasto-plastic hemisphere benchmark.

in a quasi static way. Once again this example coming from the literature was presented by Simo *et al.* [48] and is performed with the presented methods for quadratic and cubic triangles as well as for quadratic and cubic quadrilaterals. The structured quadrangular mesh is formed by 27 elements (6 elements along each edge) and the unstructured triangular mesh contains approximately 70 elements. The results are reported on Figure 13 and compared to Simo *et al.* [48] and to Betsch *et al.* [76] results. This picture gives rise to the avoidance by the full-DG formulation of the membrane and bending locking, but also of the locking resulting from the incompressible plastic behavior presents for C^0/DG triangular quadratic elements. Furthermore, except for quadratic triangles used with the C^0/DG formulation, which strongly suffer from locking, the other simulations give results in agreement with the Betsch *et al.* shell formulation. In their paper, Betsch *et al.* explained the difference with Simo formulation [48], by the difference of constitutive model. Indeed, the stress-resultant plasticity model used in [48] leads to less hardening than the J_2-flow theory used in [76] and in this work.

6.4. *Perfectly plastic cylindrical panel*

The last benchmark, presented by Belytschko *et al.* [74, 77], focuses on a cylindrical panel loaded impulsively as depicted on Figure 14(a). Perfectly plastic material properties are reported in Figure 14(b). As for the square plate example, this example is simulated using the explicit Hulbert-Chung time-integration algorithm without numerical dissipation, and using both the C^0/DG and the full-DG formulations. The results obtained with a 4×11 cubic quadrilaterals are displayed on Figure 15 and are compared to the experimental data of Belytschko *et al.* [74, 77]. This Figure shows that the presented frameworks fit well the experimental data.

6.5. *MPI benchmarks*

The efficiency of the parallel implementation is demonstrated on two examples. The efficiency of a parallel computation can be evaluated from the speed-up measurement. This number compares the time t_1 needed to perform the simulation on one processor to the time t_n needed to solve the

DOI: 10.1002/nme

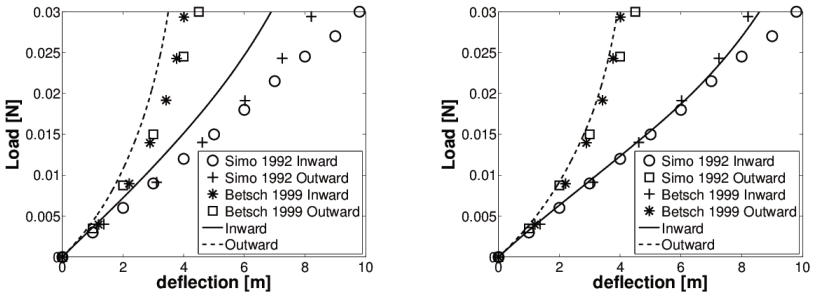

(a) C^0/DG quadratic-triangle

(b) Full-DG quadratic-triangle

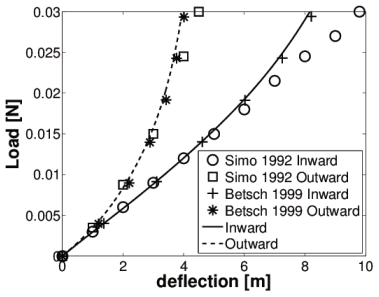

(c) C^0/DG cubic-triangle

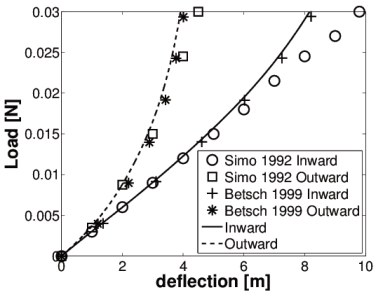

(d) Full-DG cubic-triangle

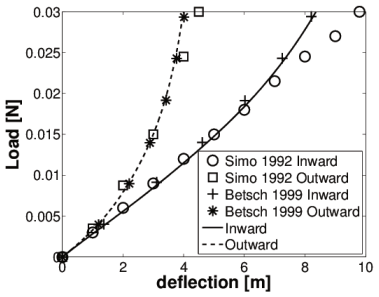

(e) C^0/DG quadratic-quadrilateral

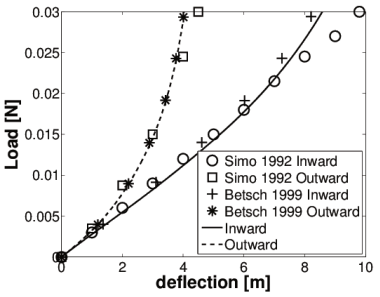

(f) Full-DG quadratic-quadrilateral

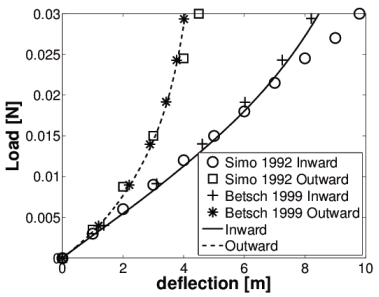

(g) C^0/DG cubic-quadrilateral

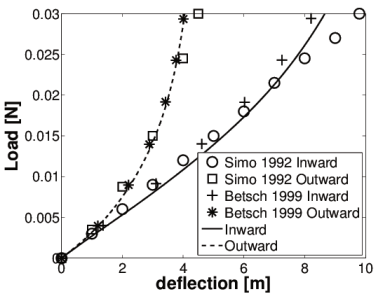

(h) Full-DG cubic-quadrilateral

Figure 13. Pinched elasto-plastic hemisphere benchmark results. Bending, membrane and plastic locking are always avoided with the full-DG method.

simulation on n processors. Ideally, the speed-up has to be equal to,

$$\text{speed-up}_{\text{theoretical}} \quad = \quad \frac{t_n}{t_1} = \frac{1}{n}\,. \tag{89}$$

DOI: 10.1002/nme

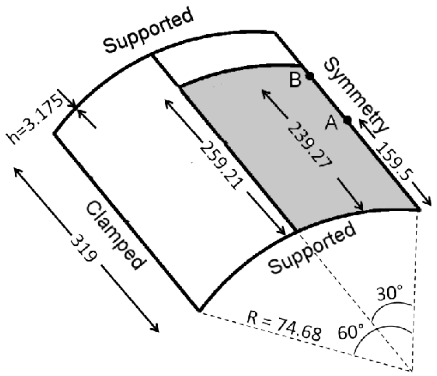

(a) Geometry (dimension in [mm])

Material properties	
Density (ρ) $[kg/m^3]$	2675
Young modulus (E) [MPa]	72400
Poisson ratio (ν) [-]	0.33
Yield stress (σ_y^0) [MPa]	303
Hardening modulus ($\bar{h}$) [MPa]	0

(b) Properties

Figure 14. Perfectly plastic cylindrical panel benchmark. The Grey part on picture (a) is the zone where a normal initial velocity of $143.51[m/s]$ is prescribed.

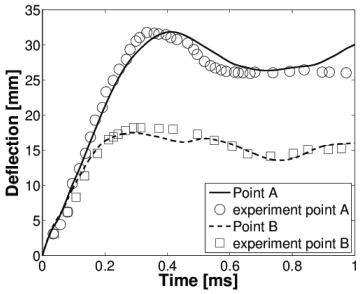

(a) C^0/DG

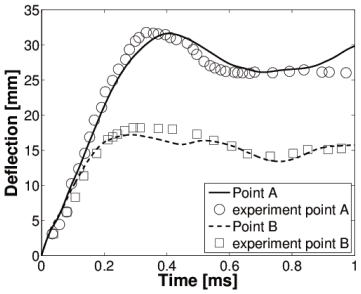

(b) Full-DG

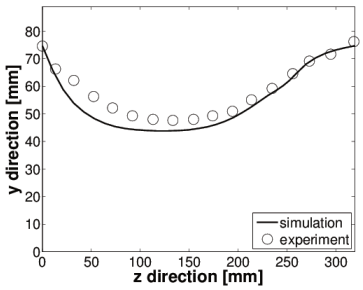

(c) Final symmetry plane outline for C^0/DG

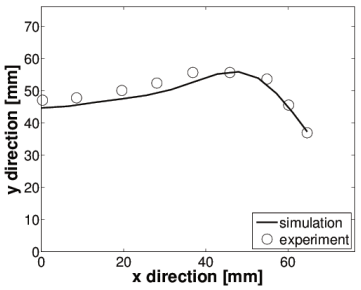

(d) Final radial section passing by point A for the full-DG

Figure 15. Perfectly plastic cylindrical panel results for C^0/DG and full-DG formulation compared to Belytschko experiments [74].

Nevertheless in practice, some data have to be exchanged during parallel computations and these MPI communications require time leading to a lower speed-up. However if the scheme is well implemented and if the cost of MPI communications is negligible, a value near the theoretical value is expected.

DOI: 10.1002/nme

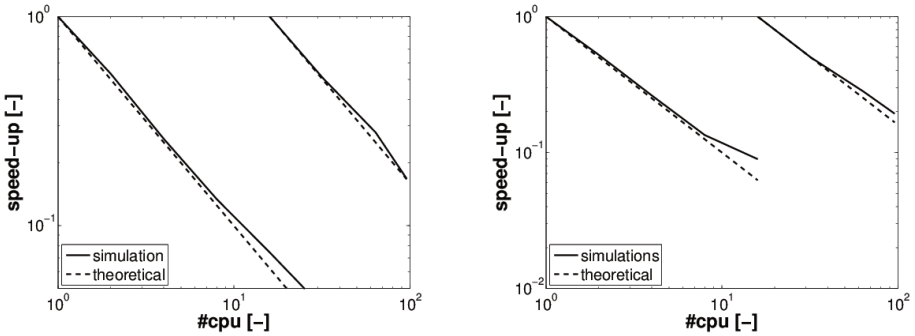

(a) Square plate (b) Cylindrical panel

Figure 16. Speed-up measured.

If the number of interface elements introduced between the mesh partitions is low compared to the number of elements of each partition, then the MPI communications are negligible. In practice a finite element mesh includes thousands of elements and is performed on tens of processors and therefore an acceptable speed-up can be obtained. To illustrate this, the two explicit benchmarks presented here-above are computed with thinner meshes. For the square plate example a 60×60 and a 120×120 elements meshes are considered, and for the cylinder, a 24×76 as well as a 48×152 elements meshes are used. As these meshes represent a large computational cost on 1 processor and as we are interested only by the speed-up measure, only 1 % of simulations are computed from 1 to 16 processors with coarser mesh and the thinner meshes are used to perform simulation from 16 to 96 processors. The speed-up ratios obtained in all cases are reported on Figure 16. For the plate example, a very good speed-up is obtained until 8 processors with the coarser mesh. After, the cost of MPI communications is not negligible and therefore the speed-up is lower than the theoretical one but it remains acceptable until 16 processors. For the cylinder example, an excellent speed-up is founded until 8 processors. Then for 16 processors the reduced number of elements by partition (around one hundred) compared to the number of interface elements (around thirty) explains the lack of efficiency. This point is highlighted by the simulation with the thinner meshes showing a speed-up near the theoretical value until 96 processors as the number of elements by partition remains large compared to the number of ghost elements. This condition is generally met for classical problems where the speed-up of the suggested method will be near the theoretical value.

6.6. Fracture application: Blast of a notched cylinder

In this application, as well as in the next one, the crack propagation of an axially notched cylindrical specimen subjected to an overpressure is studied. In particular it is shown that even if the material respects the small scale yielding assumption, *i.e.* if the plasticity remains confined around the crack tip, the recourse to an elasto-plastic model is mandatory to capture the crack speed in an accurate way.

This first example dealing with fracture was suggested by Larsson *et al.* [43] and was previously studied by the authors to validate their model of fracture for linear elastic shells [19]. The obtained results with an elastic material law were not in correlation with experiments, as mentioned by

DOI: 10.1002/nme

Larsson *et al.* , who suggested to introduce an elasto-plastic finite deformation model to study the problem in a more realistic way. The formulation developed herein is thus used to study this benchmark.

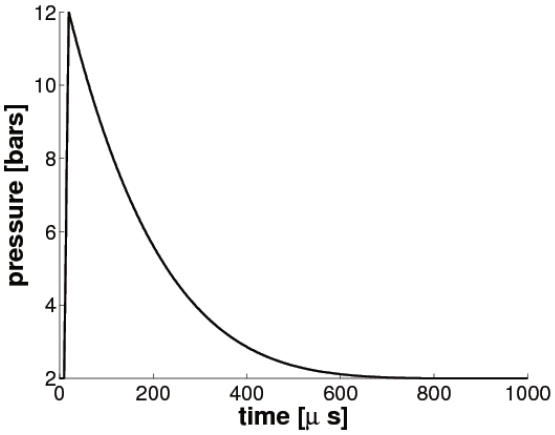

(a) Applied pressure

Geometry	
Diameter (D) [m]	1.2
Length (L) [m]	1
Thickness (h) [mm]	1
Initial crack length (l) [mm]	56
Material	
Young modulus (E) [GPa]	73.1
Poisson ratio (ν) [-]	0.33
Density (ρ) [kg/m^3]	2780
Yield stress (σ_y^0) [MPa]	350
Hardening modulus ($\bar{h}$) [MPa]	800
Fracture energy (G_c) [kJ/m^2]	19
Fracture strength (σ_c)[§] [MPa]	650 ± 65
Coupling parameter (β) [-]	1
Frictional coefficient (μ_c) [-]	0

(b) Properties

Figure 17. Model of the blasted notched cylinder.

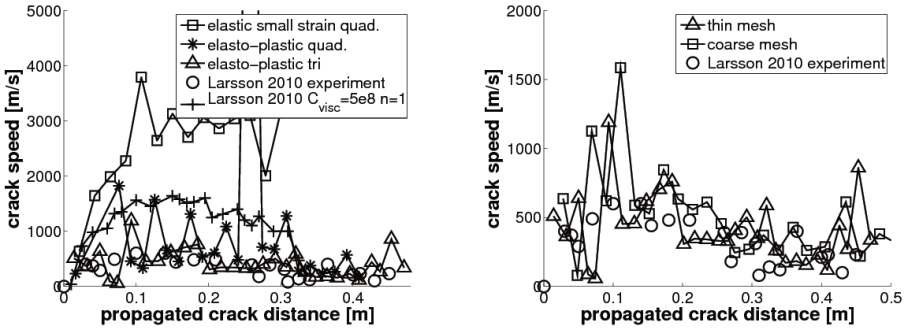

(a) Material effect

(b) Mesh effect

Figure 18. Comparison of crack speed with experimental data obtained by Larsson [43]. (a) The consideration of elasto-plastic finite deformations improve the accuracy of the simulation. (b) Although coarse meshes show a larger amplitude of oscillations the results remains in agreement with the experimental data.

The cylinder has the geometrical dimensions reported in Table 17(b). It is made of an Al2024-T3 aluminum alloy which properties are reported in Table 17(b). Note that, on the one hand the variation of fracture parameters due to surface changes is neglected here, and that on the other hand, contrarily to the elastic cases were the fracture energy is artificially increased to 67 [kJ/m^2], see [19, 43], to take into account the plastic work, the elasto-plastic formulation developed in this paper allows to use the real material values. Nevertheless, in order to avoid unphysical blow up of elements during crack propagation, the idea suggested by Zhou *et al.* [78], who used statistical distributions for the fracture strength σ_c, is considered. This strength can vary in a range around its nominal value

DOI: 10.1002/nme

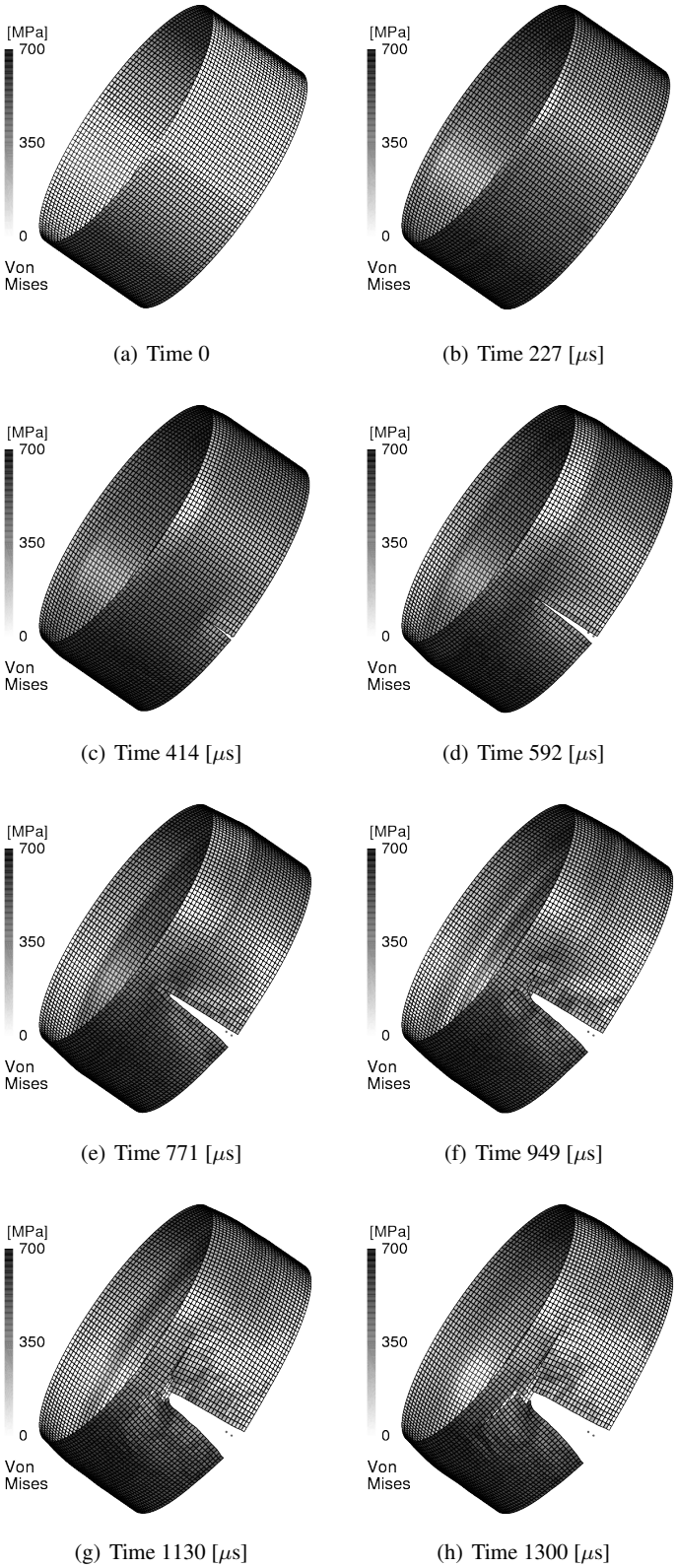

(a) Time 0

(b) Time 227 [μs]

(c) Time 414 [μs]

(d) Time 592 [μs]

(e) Time 771 [μs]

(f) Time 949 [μs]

(g) Time 1130 [μs]

(h) Time 1300 [μs]

Figure 19. The crack path remains straight for the thinnest quadrilateral mesh.

DOI: 10.1002/nme

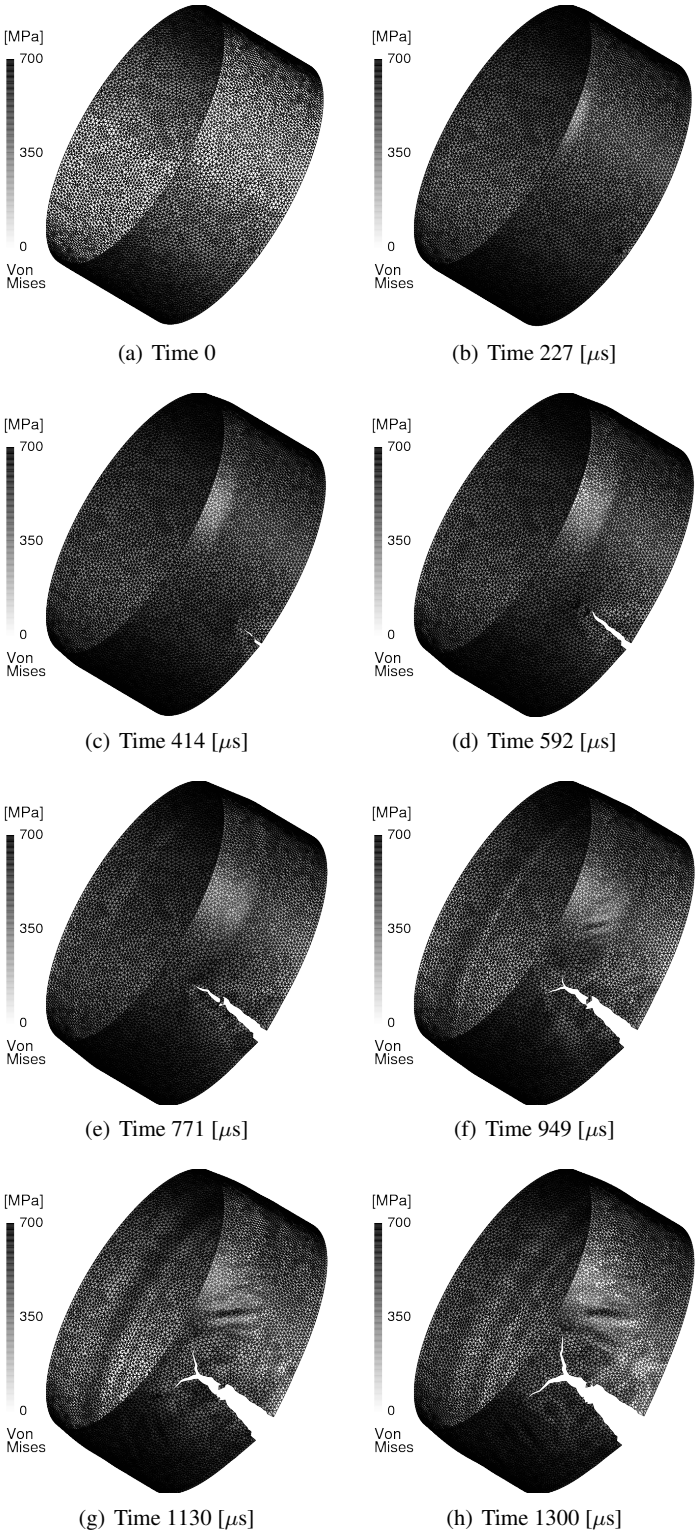

(a) Time 0 (b) Time 227 [μs]

(c) Time 414 [μs] (d) Time 592 [μs]

(e) Time 771 [μs] (f) Time 949 [μs]

(g) Time 1130 [μs] (h) Time 1300 [μs]

Figure 20. Crack propagation with the thinnest triangular mesh.

DOI: 10.1002/nme

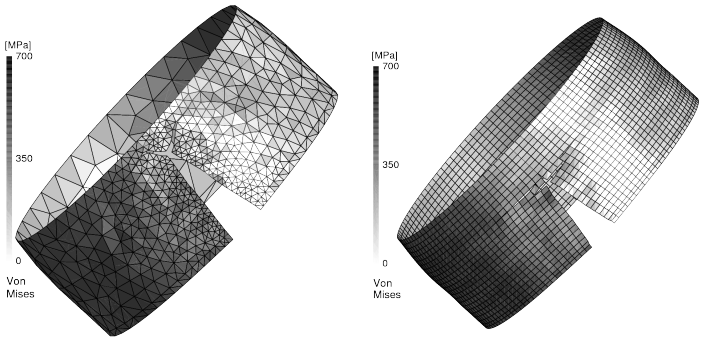

(a) Time 1300 [μs] (b) Time 1300 [μs]

Figure 21. The crack paths obtained with the coarse meshes (in this figure) are in agreement with the ones obtained with the thin meshes reported on Figures 19 and 20.

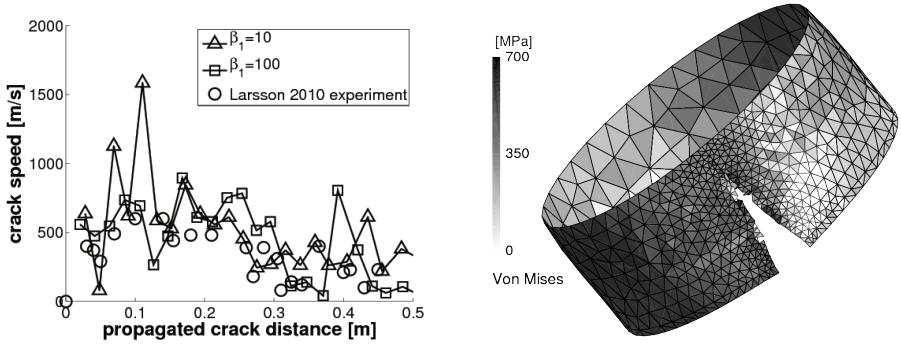

(a) Crack speed (b) Time 1300 [μs]

Figure 22. The values of the stability parameters have an influence on the initial crack speed. Furthermore, larger values of stability parameters delay the crack bifurcation at the end of the simulation.

(10% for the presented application) at each Gauss point of the interface elements and is physically justified by the material imperfections.

This notched cylinder is loaded by a blast wave, which is simulated using the internal pressure evolution depicted on Figure 17(a). The cylinder is initially pressurized at p_0 =2 [bars]. This initial pressure is applied in a quasi-static way. As the use of an implicit scheme is prohibitive due to the very thin mesh used to capture the crack speed, the dynamic relaxation presented by Papadrakakis [79], which allows performing a quasi-static analysis with an explicit dynamic scheme, is used to initiate the pressure in the cylinder, see Appendix B for a description of the method.

Taking advantage of the problem symmetry, only the top side of the cylinder is modeled by 4 different meshes: 2 bi-cubic quadrilateral meshes of respectively 3100 and 5500 elements and 2 unstructured meshes of respectively 1271 and 18536 cubic triangles. The coarse triangular mesh is refined only around the crack while the thin one is homogeneous. These meshes ensure a mesh size smaller than the cohesive size [80], which is equal to 6 [mm] in this case. The simulations are performed on 8 processors using the explicit Hulbert-Chung scheme [65] including a low numerical dissipation (spectral radius of 0.9). The stability parameters used are $\beta_1 = \beta_2 = \left(\frac{L}{h}\right)^2 \beta_3 = 10$.

Prepared using nmeauth.cls
DOI: 10.1002/nme

The crack propagation rate measured experimentally by Larsson *et al.* [43] is compared to the one obtained with the presented DG/ECL framework for linear small strain and for elasto-plastic finite deformations (with the thinner meshes) in Figure 18(a). As predicted by Larsson *et al.* the introduction of plasticity leads to results in agreement with experiments even if the speed at the beginning of the crack propagation seems faster in our model. Figure 18(b) compares the crack propagation speeds obtained for the coarse and thin meshes. Although the amplitude of oscillations are reduced with the thinnest meshes, the coarsest meshes gives results in agreement with the experiments of Larsson [43], showing that the suggested framework is quite insensitive to the mesh size to capture the crack speed.

The crack paths predicted by the simulations are shown on Figures 19 and 20, respectively for quadrilateral and triangular elements. A straight propagation is observed with quadrilateral elements as expected. With the unstructured triangular mesh, due to the heterogeneity of the mesh, the crack can locally deviate, but the direction remains straight until bifurcating when reaching the clamped parts, as observed by the experimental data. As expected, an unstructured mesh converges toward the physical solution. Furthermore, the final configuration obtained with the coarser quadrilateral and triangular meshes are depicted on Figure 21. These final configurations are in agreement with the ones obtained with the thinner meshes, which confirms that the suggested approach is more insensitive to the mesh size than what is usually reported in the literature.

Finally, the effect of the stability parameters is also studied on the coarse triangular mesh. As illustrated on Figure 22(a), the recourse to larger values of stability parameters ($\beta_1 = \beta_2 = \left(\frac{L_c}{h}\right)^2 \beta_3 = 100$) decreases the crack speed at the beginning of the simulation, but these values delay the crack bifurcation, as depicted on Figure 22(b). A thinner mesh would reduce this effect.

6.7. *Fracture application: Crack propagation in a notched detonation tube*

The second example focuses on the crack propagation due to an internal detonation pressure in an axially notched tube whose geometrical and material properties (Al6061-T6) are depicted on Figure 23. This application was studied in the literature by J.-H. Song *et al.* [55] using the XFEM method, and by T. Chao [81], who performed experiments. We report herein the results obtained using the full-DG/ECL framework. The detonation is modeled by prescribing the inner pressure over time following [81],

$$p(x,t) = \begin{cases} 0 & t \leq \frac{x}{v^{cj}} \\ p^{cj} e^{\frac{-\left(t-\frac{x}{v^{cj}}\right)}{\frac{3x}{v^{cj}}}} & t > \frac{x}{v^{cj}} \end{cases} \tag{90}$$

where, $p^{cj} = 6.2$ [MPa] and $v^{cj} = 2390$ [m/s] are respectively the Chapmand-Jouguet pressure and the detonation wave propagation velocity. The spatial coordinate x is the distance between the detonation source and the material point where the pressure is computed[¶]. In the experiments reported by J.-H. Song *et al.* [55] the notch is only 0.58 [mm] deep, but we consider in our model a notch going all through the thickness, as it seems having a few influence on the results. Finally

[¶]In our simulations we do not model, neither the detonation process, nor the flanges that support the tube. Therefore the coordinate $x = 0$ is taken at the left extremity of the tube as depicted on Figure 23 and not at the flange origin as in [55]. The time reported should then be translated by $t_0 = 20.92$ [μs] when comparing our results with [55].

DOI: 10.1002/nme

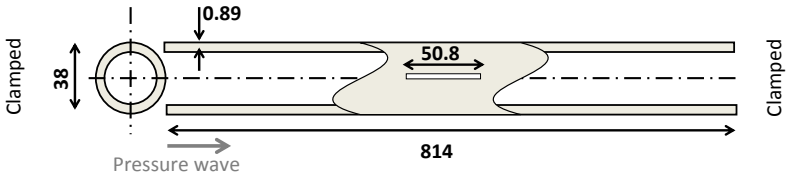

(a) Geometry (dimension in [mm])

Al6061-T6	
Density (ρ) [kg/m^3]	2780
Young modulus (E) [MPa]	69000
Poisson ratio (ν) [-]	0.3
Yield stress (σ_y^0) [MPa]	275
Hardening modulus ($\overline{h}$) [MPa]	640
Fracture energy (G_c) [kJ/m^2]	19
Fracture strength (σ_c) [MPa]	495 ± 25
Coupling parameter (β) [-]	1
Frictional coefficient (μ_c) [-]	0

(b) Properties

Figure 23. Setup for the study of crack propagation in a notched detonation tube, sketch following [55].

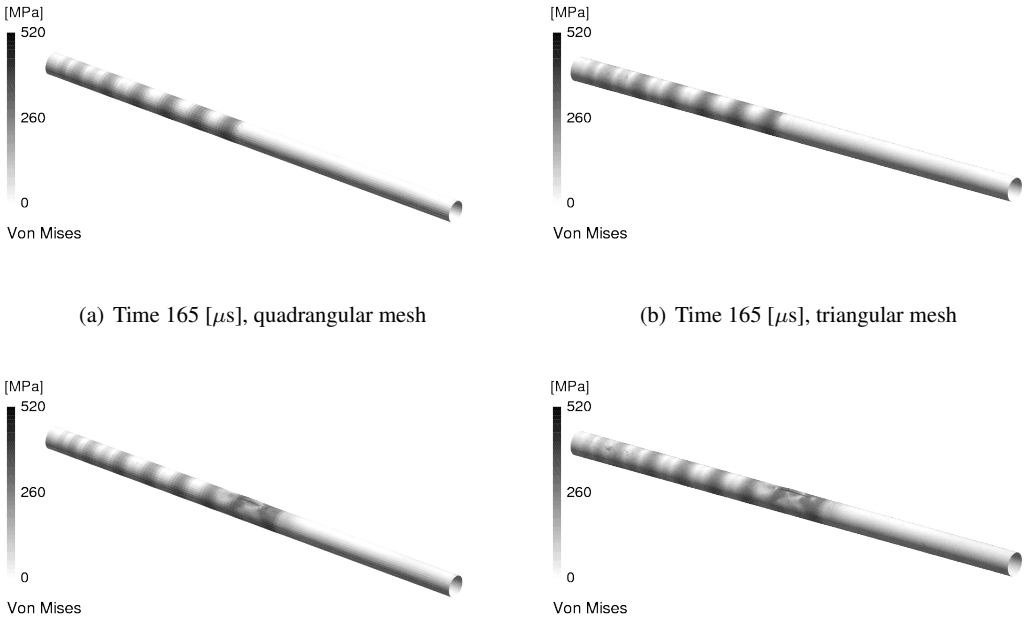

(a) Time 165 [μs], quadrangular mesh

(b) Time 165 [μs], triangular mesh

(c) Time 200 [μs], quadrangular mesh

(d) Time 200 [μs], triangular mesh

Figure 24. A stress wave, induced by the pressure wave, propagates from the left to the right extremities of the tube.

Prepared using nmeauth.cls
DOI: 10.1002/nme

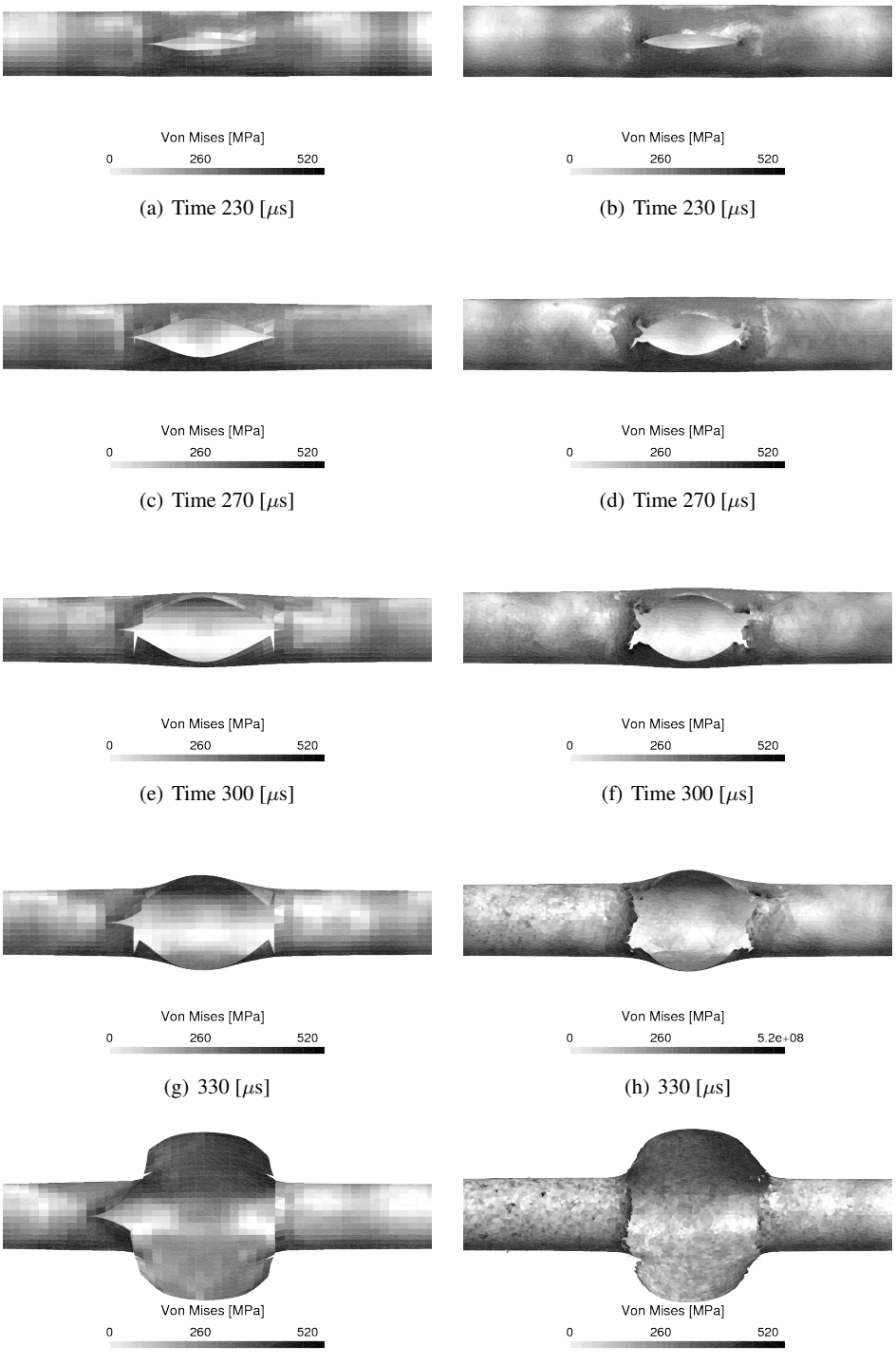

(a) Time 230 [μs] (b) Time 230 [μs]

(c) Time 270 [μs] (d) Time 270 [μs]

(e) Time 300 [μs] (f) Time 300 [μs]

(g) 330 [μs] (h) 330 [μs]

(i) Time 400 [μs] (j) Time 400 [μs]

Figure 25. The crack starts to propagate straightly in both directions and then bifurcates to propagate radially for the quadrangular mesh (left) and for triangular mesh (right). The quadrangular mesh captures the experimentally observed backward straight crack propagation which continues after the backward crack bifurcation.

Prepared using nmeauth.cls
DOI: 10.1002/nme

the last difference with the numerical model of J.-H. Song *et al.* [55] is the recourse in this paper to a local fracture criterion based on an effective stress in place of a non local criterion based on the equivalent plastic strain in [55]. As we use a local model, we consider a higher fracture strength. To determine our fracture strength we follow the work of P. Zavattieri [57] and choose $\sigma_c = 1.8\sigma_y^0$. To introduce inhomogeneities in the simulation this parameter belongs in a 5% range, following a normal distribution as suggested by J.-H. Song *et al.* [55].

In this paper this benchmark is performed with 2 different meshes. The first one has 4670 third-order quadrangular elements and the second one is formed by 34888 second-order triangular elements.

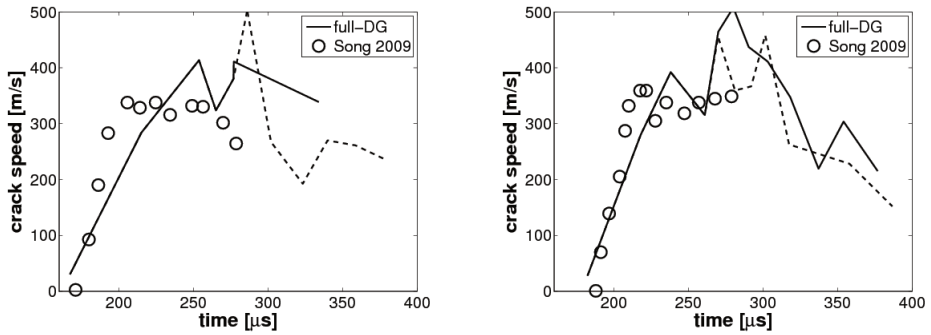

(a) Backward crack (b) Forward crack

Figure 26. The crack speed observed with the quadrangular meshes is in agreement with the one computed by J.-H. Song *et al.* [55]. Dot lines are used when the crack bifurcates in two branches.

The pressure wave induces a stress wave propagating from the left to the right of the tube with an amplitude lower than the fracture strength. When the stress wave reaches the notch, a stress concentration occurs at the crack tips as illustrated on Figure 24. This stress concentration is large enough to induce the straight propagation of the crack at both extremities of the notch as shown on Figure 25. Then the backward and the forward cracks bifurcate (approximately at the same time) and propagate radially. As the backward crack is firstly hit by the stress wave its propagates straight during a longer time and therefore on a longer distance, in agreement to what was experimentally observed. When the bifurcation occurs the forward crack bifurcates and the two branches propagate radially. This phenomenon is also observed for the backward crack but the crack keeps also a straight propagation for the quadrangular mesh. This straight propagation is also observed experimentally (see [81, 55]). Therefore in this case the use of quadrangular elements seems better to capture the crack path. After bifurcation the cracks continue to propagate radially until the simulation is stopped. The speed of the crack propagation during the whole process, is illustrated on Figure 26 for the quadrangular mesh. This speed is in agreement with the one obtained by J.-H. Song [55] until 300 [μs]. At that time, the crack bifurcates and experimental results are lacking. On this picture we represent in a dotted line the second radial crack which appears after the bifurcation.

DOI: 10.1002/nme

7. CONCLUSIONS

This paper focuses on the extension to elasto-plasticity and finite deformations of a framework combining the full-discontinuous Galerkin formulation of shells with the extrinsic cohesive law. The obvious interest of the framework is its ability to simulate crack propagation as the recourse to a discontinuous formulation allows inserting cohesive elements on the fly during the simulation without any modification of the mesh topology.

This method was implemented in parallel to be able to perform fracture applications with very fine meshes. Furthermore, the full-discontinuous Galerkin method can also be used to perform parallel computations. Indeed, such a formulation can be used to weakly guarantee the continuity between two partitions of two different processors with an excellent speed-up.

Finally, the presented full-DG formulation for elasto-plastic finite deformations of shells was applied on usual thin body benchmarks, and has been shown to give accurate results. When combined to the extrinsic cohesive law, this formulation has been shown to predict the crack propagation with a good agreement with experimental data on two different applications. Furthermore the observed crack speed, which is limited by the plasticity, is well capture when having recourse to elasto-plastic material law. The developed framework allows accounting for the plasticity even at interfaces between elements which is a suitable advantage compare to the recourse to an intrinsic cohesive law leading to an elastic response at interfaces. Furthermore, contrarily to linear elastic fracture models, no modification of the material parameters of the cohesive law inherent to the elastic assumption was required. However the presented framework is suitable only for small scale yielding and other improvements are necessary to simulate crack propagation in ductile materials.

REFERENCES

1. Hillerborg A, Modéer M, Petersson PE. Analysis of crack formation and crack growth in concrete by means of fracture mechanics and finite elements. *Cement and Concrete Research* 1976; **6**(6):773 – 781, doi: 10.1016/0008-8846(76)90007-7. URL http://www.sciencedirect.com/science/article/pii/0008884676900077.
2. Dugdale DS. Yielding of steel sheets containing slits. *Journal of the Mechanics and Physics of Solids* May 1960; **8**(2):100–104. URL http://www.sciencedirect.com/science/article/B6TXB-46J03KX-2K/2/764967fc0699800cd276b09abd568f3e.
3. Barenblatt G. The mathematical theory of equilibrium cracks in brittle fracture. Elsevier, 1962; 55–129. URL http://www.sciencedirect.com/science/article/B7RNC-4S867RJ-6/2/24d2fbaac93457d135f935d6cfa35836.
4. Needleman A. A continuum model for void nucleation by inclusion debonding. *Journal of Applied Mechanics* 1987; **54**:525–531.
5. Needleman A. An analysis of decohesion along an imperfect interface. *International Journal of Fracture* 1990; **42**:21–40. URL http://dx.doi.org/10.1007/BF00018611.
6. Tvergaard V, Hutchinson JW. The relation between crack growth resistance and fracture process parameters in elastic-plastic solids. *Journal of the Mechanics and Physics of Solids* 1992; **40**(6):1377 – 1397, doi: 10.1016/0022-5096(92)90020-3. URL http://www.sciencedirect.com/science/article/pii/0022509692900203.
7. Scheider I, Brocks W. Simulation of cup-cone fracture using the cohesive model. *Engineering Fracture Mechanics* 2003; **70**(14):1943–1961. URL http://www.sciencedirect.com/science/article/B6V2R-48KF7Y8-1/2/3ebd02d524ce26db2ca47735385023d9.

DOI: 10.1002/nme

8. Tvergaard V. Effect of fibre debonding in a whisker-reinforced metal. *Materials Science and Engineering: A* 1990; **125**(2):203 – 213, doi:10.1016/0921-5093(90)90170-8. URL http://www.sciencedirect.com/science/article/pii/0921509390901708.
9. Needleman A. An analysis of tensile decohesion along an interface. *Journal of the Mechanics and Physics of Solids* 1990; **38**(3):289 – 324, doi:10.1016/0022-5096(90)90001-K. URL http://www.sciencedirect.com/science/article/pii/002250969090001K.
10. Tvergaard V, Hutchinson JW. The influence of plasticity on mixed mode interface toughness. *Journal of the Mechanics and Physics of Solids* 1993; **41**(6):1119 – 1135, doi:10.1016/0022-5096(93)90057-M. URL http://www.sciencedirect.com/science/article/pii/002250969390057M.
11. Tvergaard V, Hutchinson JW. Effect of strain-dependent cohesive zone model on predictions of crack growth resistance. *International Journal of Solids and Structures* 1996; **33**(20-22):3297–3308–. URL http://www.sciencedirect.com/science/article/B6VJS-3VTSPVJ-S/2/71976b9761cf9bd81d308e234b91cf3b.
12. Klein PA, Foulk JW, Chen EP, Wimmer SA, Gao HJ. Physics-based modeling of brittle fracture: cohesive formulations and the application of meshfree methods. *Theoretical and Applied Fracture Mechanics* Dec 2001; **37**(1-3):99–166. URL http://www.sciencedirect.com/science/article/B6V55-4465TB7-1/2/a970f5c2f6dbdc54bc6ba3eead7729d4.
13. Seagraves A, Radovitzky R. Advances in cohesive zone modeling of dynamic fracture. *Dynamic Failure of Materials and Structures*, Shukla A, Ravichandran G, Rajapakse YD (eds.). Springer US, 2010; 349–405. URL http://dx.doi.org/10.1007/978-1-4419-0446-1_12.
14. Camacho GT, Ortiz M. Computational modelling of impact damage in brittle materials. *International Journal of Solids and Structures* 1996; **33**(20-22):2899–2938–. URL http://www.sciencedirect.com/science/article/B6VJS-3VTSPVJ-3/2/98fe3c31d0cee8e029d78d1631c6bbdd.
15. Pandolfi A, Krysl P, Ortiz M. Finite element simulation of ring expansion and fragmentation: The capturing of length and time scales through cohesive models of fracture. *International Journal of Fracture* 1999; **95**(1):279–297. URL http://dx.doi.org/10.1023/A:1018672922734.
16. Ortiz M, Ortiz M, Pandolfi A. Finite-deformation irreversible cohesive elements for three-dimensional crack propagation analysis. *International Journal for Numerical Methods in Engineering* 2000; **44**:44–1267.
17. Cirak F, Deiterding R, Mauch SP. Large-scale fluid-structure interaction simulation of viscoplastic and fracturing thin-shells subjected to shocks and detonations. *Computers & Structures* 2007; **85**(11-14):1049–1065–. URL http://www.sciencedirect.com/science/article/B6V28-4MV19R2-2/2/31dc7c2542ae69498e68b2ee13aa88fe.
18. Cirak F, Ortiz M, Pandolfi A. A cohesive approach to thin-shell fracture and fragmentation. *Computer Methods in Applied Mechanics and Engineering* 2005; **194**(21-24):2604–2618. URL http://www.sciencedirect.com/science/article/B6V29-4FBW600-4/2/06c015e841d7fba329790dd872c4986e.
19. Becker G, Geuzaine C, Noels L. A one field full discontinuous galerkin method for kirchhoff-love shells applied to fracture mechanics. *Computer Methods in Applied Mechanics and Engineering* 2011; **200**:3223–3241, doi:DOI:10.1016/j.cma.2011.07.008. URL http://www.sciencedirect.com/science/article/pii/S0045782511002490.
20. Cocburn B. *Discontinuous Galerkin methods for convection-dominated problems. In High-Order Methods for Computational Physics*, *Lecture Notes in Computational Sciences and Engineering*, vol. 11. Berlin : Springer, 1999.
21. Cockburn B. Discontinuous galerkin methods. *ZAMM - Journal of Applied Mathematics and Mechanics / Zeitschrift far Angewandte Mathematik und Mechanik* 2003; **83**(11):731–754, doi:10.1002/zamm.200310088. URL http://dx.doi.org/10.1002/zamm.200310088.
22. Arnold DN, Brezzi F, Cockburn B, Marini LD. Unified analysis of discontinuous galerkin methods for elliptic problems. *SIAM Journal on Numerical Analysis* 2002; **39**(5):1749–1779–. URL http://www.jstor.org/stable/4101034.
23. Hansbo P, Larson MG. A discontinuous galerkin method for the plate equation. *Calcolo* 2002; **39**(1):41–59–. URL http://dx.doi.org/10.1007/s100920200001.
24. Lew A, Neff P, Sulsky D, Ortiz M. Optimal bv estimates for a discontinuous galerkin method for linear elasticity. *Appl Math Res Express* 2004; **2004**(3):73–106–. URL http://amrx.oxfordjournals.org/cgi/content/abstract/2004/3/73.
25. Celiker F, Cockburn B, Stolarski HK. Locking-free optimal discontinuous galerkin methods for timoshenko beams. *SIAM Journal on Numerical Analysis* 2006; **44**(6):2297–2325–. URL http://link.aip.org/link/?SNA/44/2297/1.

DOI: 10.1002/nme

26. Guzey S, Stolarski HK, Cockburn B, Tamma KK. Design and development of a discontinuous galerkin method for shells. *Computer Methods in Applied Mechanics and Engineering* 2006; **195**(25-28):3528–3548. URL http://www.sciencedirect.com/science/article/B6V29-4H4T0NX-5/2/fe6bc096c9886ac34cbf27f86e02f31b.
27. Eyck AT, Lew A. Discontinuous galerkin methods for non-linear elasticity. *International Journal for Numerical Methods in Engineering* 2006; **67**(9):1204–1243. URL http://dx.doi.org/10.1002/nme.1667.
28. S Guzey HKS B Cockburn. The embedded discontinuous galerkin method: application to linear shell problems. *International Journal for Numerical Methods in Engineering* 2007; **70**(7):757–790. URL http://dx.doi.org/10.1002/nme.1893.
29. Wells GN, Dung NT. A c0 discontinuous galerkin formulation for kirchhoff plates. *Computer Methods in Applied Mechanics and Engineering* 2007; **196**(35-36):3370–3380. URL http://www.sciencedirect.com/science/article/B6V29-4NG3T6W-3/2/0409f57fd4b386e71e9ee076e1c0ffed.
30. Lew A, Eyck A, Rangarajan R. Some applications of discontinuous galerkin methods in solid mechanics. *IUTAM Symposium on Theoretical, Computational and Modelling Aspects of Inelastic Media* 2008; :227–236URL http://dx.doi.org/10.1007/978-1-4020-9090-5_21.
31. Eyck AT, Celiker F, Lew A. Adaptive stabilization of discontinuous galerkin methods for nonlinear elasticity: Motivation, formulation, and numerical examples. *Computer Methods in Applied Mechanics and Engineering* Aug 2008; **197**(45-48):3605–3622. URL http://www.sciencedirect.com/science/article/B6V29-4RY6WKK-1/2/c484a571e4c532aa6448233fe12e43a6.
32. Noels L, Radovitzky R. An explicit discontinuous galerkin method for non-linear solid dynamics: Formulation, parallel implementation and scalability properties. *International Journal for Numerical Methods in Engineering* 2008; **74**(9):1393–1420. URL http://dx.doi.org/10.1002/nme.2213.
33. Noels L, Radovitzky R. A new discontinuous galerkin method for kirchhoff-love shells. *Computer Methods in Applied Mechanics and Engineering* 2008; **197**(33-40):2901–2929. URL http://www.sciencedirect.com/science/article/B6V29-4RSRDCT-1/2/9b24e4b7bb547bf5c27d28e6b0898610.
34. Noels L. A discontinuous galerkin formulation of non-linear kirchhoff-love shells. *International Journal for Numerical Methods in Engineering* 2009; **78**(3):296–323. URL http://dx.doi.org/10.1002/nme.2489.
35. Shen Y, Lew A. An optimally convergent discontinuous galerkin-based extended finite element method for fracture mechanics. *International Journal for Numerical Methods in Engineering* 2010; **82**(6):716–755. URL http://dx.doi.org/10.1002/nme.2781.
36. Engel G, Garikipati K, Hughes TJR, Larson MG, Mazzei L, Taylor RL. Continuous/discontinuous finite element approximations of fourth-order elliptic problems in structural and continuum mechanics with applications to thin beams and plates, and strain gradient elasticity. *Computer Methods in Applied Mechanics and Engineering* Jul 2002; **191**(34):3669–3750. URL http://www.sciencedirect.com/science/article/B6V29-45SRHD8-1/2/464ae949db39e8ad8352b23195051109.
37. Wells GN, Garikipati K, Molari L. A discontinuous galerkin formulation for a strain gradient-dependent damage model. *Computer Methods in Applied Mechanics and Engineering* 2004; **193**(33-35):3633 – 3645, doi:DOI:10.1016/j.cma.2004.01.020. URL http://www.sciencedirect.com/science/article/pii/S0045782504000921.
38. Molari L, Wells GN, Garikipati K, Ubertini F. A discontinuous galerkin method for strain gradient-dependent damage: Study of interpolations and convergence. *Computer Methods in Applied Mechanics and Engineering* 2006; **195**(13-16):1480 – 1498, doi:DOI:10.1016/j.cma.2005.05.026. URL http://www.sciencedirect.com/science/article/pii/S0045782505002914, a Tribute to Thomas J.R. Hughes on the Occasion of his 60th Birthday.
39. Becker G, Noels L. A fracture framework for euler-bernoulli beams based on a full discontinuous galerkin formulation/extrinsic cohesive law combination. *International Journal for Numerical Methods in Engineering* 2011; **85**(10):1227–1251, doi:10.1002/nme.3008. URL http://dx.doi.org/10.1002/nme.3008.
40. Mergheim J, Kuhl E, Steinmann P. A hybrid discontinuous galerkin/interface method for the computational modelling of failure. *Communications in Numerical Methods in Engineering* 2004; **20**(7):511–519. URL http://dx.doi.org/10.1002/cnm.689.
41. Prechtel M, Ronda P, Janisch R, Hartmaier A, Leugering G, Steinmann P, Stingl M. Simulation of fracture in heterogeneous elastic materials with cohesive zone models. *International Journal of Fracture* 2011; **168**:15–29. URL http://dx.doi.org/10.1007/s10704-010-9552-z, 10.1007/s10704-010-9552-z.
42. Radovitzky R, Seagraves A, Tupek M, Noels L. A scalable 3d fracture and fragmentation algorithm based on a hybrid, discontinuous galerkin, cohesive element method. *Computer Methods in Applied Mechanics and Engineering* 2011; **200**:326–344, doi:DOI:10.1016/j.cma.2010.08.014. URL http://www.sciencedirect.

com/science/article/B6V29-50XS6BT-2/2/5bc8ab13cb73edc50fb1c2a4fb7439d3.

43. Larsson R, Mediavilla J, Fagerstrm M. Dynamic fracture modeling in shell structures based on xfem. *Int. J. Numer. Meth. Engng.* 2011; **86**(4-5):499–527, doi:10.1002/nme.3086. URL http://dx.doi.org/10.1002/nme.3086.
44. Simo JC, Fox DD. On stress resultant geometrically exact shell model. part i: formulation and optimal parametrization. *Comput. Methods Appl. Mech. Eng.* 1989; **72**(3):267–304.
45. Simo JC, Fox DD, Rifai MS. On a stress resultant geometrically exact shell model. part ii: the linear theory; computational aspects. *Comput. Methods Appl. Mech. Eng.* 1989; **73**(1):53–92.
46. Simo J, Fox D, Rifai M. On a stress resultant geometrically exact shell model. part iii: Computational aspects of the nonlinear theory. *Computer Methods in Applied Mechanics and Engineering* 1990; **79**(1):21 – 70, doi:DOI:10.1016/0045-7825(90)90094-3. URL http://www.sciencedirect.com/science/article/B6V29-47XSWMP-3/2/a7d8adf2ee1bde1ca1943b2179e27a9a.
47. Simo JC, Rifai MS, Fox DD. On a stress resultant geometrically exact shell model. part iv: Variable thickness shells with through-the-thickness stretching. *Computer Methods in Applied Mechanics and Engineering* 1990; **81**(1):91 – 126, doi:DOI:10.1016/0045-7825(90)90143-A. URL http://www.sciencedirect.com/science/article/B6V29-4808WRV-30/2/57f79632994b5829488baed916c1a998.
48. Simo J, Kennedy J. On a stress resultant geometrically exact shell model. part v. nonlinear plasticity: formulation and integration algorithms. *Computer Methods in Applied Mechanics and Engineering* 1992; **96**(2):133 – 171, doi:DOI:10.1016/0045-7825(92)90129-8. URL http://www.sciencedirect.com/science/article/B6V29-47YJHG3-T/2/9de358cec2b4c5890934d756457471dc.
49. Cirak F, Ortiz M, Schrder P. Subdivision surfaces: a new paradigm for thin-shell finite-element analysis. *International Journal for Numerical Methods in Engineering* 2000; **47**(12):2039–2072, doi:10.1002/(SICI)1097-0207(20000430)47:12⟨2039::AID-NME872⟩3.0.CO;2-1. URL http://dx.doi.org/10.1002/(SICI)1097-0207(20000430)47:12⟨2039::AID-NME872⟩3.0.CO;2-1.
50. Cirak F, Ortiz M. Fully c1-conforming subdivision elements for finite deformation thin-shell analysis. *International Journal for Numerical Methods in Engineering* 2001; **51**(7):813–833, doi:10.1002/nme.182. URL http://dx.doi.org/10.1002/nme.182.
51. Deiterding R, Radovitzky R, Mauch S, Noels L, Cummings J, Meiron D. A virtual test facility for the efficient simulation of solid material response under strong shock and detonation wave loading. *Engineering with Computers* 2006; **22**(3):325–347–. URL http://dx.doi.org/10.1007/s00366-006-0043-9.
52. Cuitino A, Ortiz M. A material-independent method for extending stress update algorithms from small-strain plasticity to finite plasticity with multiplicative kinematics. *Engineering Computations* 1992; **9**:437–451.
53. Areias PMA, Belytschko T. Non-linear analysis of shells with arbitrary evolving cracks using xfem. *International Journal for Numerical Methods in Engineering* 2005; **62**(3):384–415, doi:10.1002/nme.1192. URL http://dx.doi.org/10.1002/nme.1192.
54. Areias PMA, Song JH, Belytschko T. Analysis of fracture in thin shells by overlapping paired elements. *Computer Methods in Applied Mechanics and Engineering* 2006; **195**(41-43):5343–5360–. URL http://www.sciencedirect.com/science/article/B6V29-4J555VV-5/2/15a96d0ad797df5739a5fc252ad44044.
55. Song JH, Belytschko T. Dynamic fracture of shells subjected to impulsive loads. *Journal of Applied Mechanics* 2009; **76**(5):051301, doi:10.1115/1.3129711. URL http://link.aip.org/link/?AMJ/76/051301/1.
56. Zavattieri P. Modeling of crack propagation in thin-walled structures. *Mecanica Computacional* 2004; **XXIII**:209–228.
57. Zavattieri PD. Modeling of crack propagation in thin-walled structures using a cohesive model for shell elements. *J. Appl. Mech.* Nov 2006; **73**(6):948–958. URL http://link.aip.org/link/?AMJ/73/948/1.
58. Corigliano A, Cacchione F, Frangi A, Zerbini S. Numerical modelling of impact rupture in polysilicon microsystems. *Computational Mechanics* 2008; **42**:251–259. URL http://dx.doi.org/10.1007/s00466-007-0231-5, 10.1007/s00466-007-0231-5.
59. J F Molinari RRARFZ G Gazonas. The cohesive element approach to dynamic fragmentation: the question of energy convergence. *International Journal for Numerical Methods in Engineering* 2007; **69**(3):484–503. URL http://dx.doi.org/10.1002/nme.1777.
60. Li H, Chandra N. Analysis of crack growth and crack-tip plasticity in ductile materials using cohesive zone models. *International Journal of Plasticity* 2003; **19**(6):849–882–. URL http://www.sciencedirect.com/science/article/B6TWX-45DF7DC-2/2/5b0f96fbff717dba3403fe5e02295e46.
61. Pandolfi A, Ortiz M. An efficient adaptive procedure for three-dimensional fragmentation simulations. *Engineering with Computers* Aug 2002; **18**(2):148–159. URL http://dx.doi.org/10.1007/s003660200013.

62. Papoulia KD, Sam CH, Vavasis SA. Time continuity in cohesive finite element modeling. *International Journal for Numerical Methods in Engineering* 2003; **58**(5):679–701. URL http://dx.doi.org/10.1002/nme.778.
63. Zhang ZJ, Paulino GH, Celes W. Extrinsic cohesive modelling of dynamic fracture and microbranching instability in brittle materials. *International Journal for Numerical Methods in Engineering* 2007; **72**(8):893–923. URL http://dx.doi.org/10.1002/nme.2030.
64. Geuzaine C, Remacle JF. Gmsh: A 3-d finite element mesh generator with built-in pre- and post-processing facilities. *International Journal for Numerical Methods in Engineering* 2009; **79**(11):1309–1331. URL http://dx.doi.org/10.1002/nme.2579.
65. Hulbert GM, Chung J. Explicit time integration algorithms for structural dynamics with optimal numerical dissipation. *Computer Methods in Applied Mechanics and Engineering* 1996; **137**(2):175 – 188, doi:DOI:10.1016/S0045-7825(96)01036-5. URL http://www.sciencedirect.com/science/article/B6V29-3WFNRDY-5/2/2ec79b924e3dd1b9231ffe40c6a40306.
66. Karypis G, Kumar V. A fast and high quality multilevel scheme for partitioning irregular graphs. *SIAM Journal on Scientific Computing* 1998; **20**(1):359–392. URL http://link.aip.org/link/SJOCE3/v20/i1/p359/s1&Agg=doi.
67. Balay S, Brown J, , Buschelman K, Eijkhout V, Gropp WD, Kaushik D, Knepley MG, McInnes LC, Smith BF, *et al.*. PETSc users manual. *Technical Report ANL-95/11 - Revision 3.1*, Argonne National Laboratory 2010.
68. Balay S, Brown J, Buschelman K, Gropp WD, Kaushik D, Knepley MG, McInnes LC, Smith BF, Zhang H. PETSc Web page 2011. URL http://www.mcs.anl.gov/petsc, http://www.mcs.anl.gov/petsc.
69. Basar Y, Ding Y. Finite-rotation shell elements for the analysis of finite-rotation shell problems. *International Journal for Numerical Methods in Engineering* 1992; **34**(1):165–169, doi:10.1002/nme.1620340109. URL http://dx.doi.org/10.1002/nme.1620340109.
70. Buechter N, Ramm E. Shell theory versus degeneration-a comparison in large rotation finite element analysis. *International Journal for Numerical Methods in Engineering* 1992; **34**(1):39–59, doi:10.1002/nme.1620340105. URL http://dx.doi.org/10.1002/nme.1620340105.
71. Sansour C, Bocko J. On hybrid stress, hybrid strain and enhanced strain finite element formulations for a geometrically exact shell theory with drilling degrees of freedom. *International Journal for Numerical Methods in Engineering* 1998; **43**(1):175–192, doi:10.1002/(SICI)1097-0207(19980915)43:1⟨175::AID-NME448⟩3.0.CO;2-9. URL http://dx.doi.org/10.1002/(SICI)1097-0207(19980915)43:1⟨175::AID-NME448⟩3.0.CO;2-9.
72. Sansour C, Kollmann FG. Families of 4-node and 9-node finite elements for a finite deformation shell theory. an assesment of hybrid stress, hybrid strain and enhanced strain elements. *Computational Mechanics* 2000; **24**:435–447. URL http://dx.doi.org/10.1007/s004660050003, 10.1007/s004660050003.
73. Areias PMA, Song JH, Belytschko T. A finite-strain quadrilateral shell element based on discrete kirchhoff-love constraints. *International Journal for Numerical Methods in Engineering* 2005; **64**(9):1166–1206, doi:10.1002/nme.1389. URL http://dx.doi.org/10.1002/nme.1389.
74. Belytschko T, Lin JI, Chen-Shyh T. Explicit algorithms for the nonlinear dynamics of shells. *Computer Methods in Applied Mechanics and Engineering* 1984; **42**(2):225 – 251, doi:DOI:10.1016/0045-7825(84)90026-4. URL http://www.sciencedirect.com/science/article/pii/0045782584900264.
75. Swaddiwudhipong S, Liu ZS. Dynamic response of large strain elasto-plastic plate and shell structures. *Thin-Walled Structures* 1996; **26**(4):223 – 239, doi:DOI:10.1016/0263-8231(96)00031-6. URL http://www.sciencedirect.com/science/article/pii/0263823196000316.
76. Betsch P, Stein E. Numerical implementation of multiplicative elasto-plasticity into assumed strain elements with application to shells at large strains. *Computer Methods in Applied Mechanics and Engineering* 1999; **179**(3-4):215 – 245, doi:DOI:10.1016/S0045-7825(99)00063-8. URL http://www.sciencedirect.com/science/article/pii/S0045782599000638.
77. Belytschko T, Wong BL, Plaskacz EJ. Fission-fusion adaptivity in finite elements for nonlinear dynamics of shells. *Computers & Structures* 1989; **33**(5):1307 – 1323, doi:DOI:10.1016/0045-7949(89)90468-9. URL http://www.sciencedirect.com/science/article/pii/0045794989904689.
78. Zhou F, Molinari JF. Stochastic fracture of ceramics under dynamic tensile loading. *International Journal of Solids and Structures* 2004; **41**(22-23):6573 – 6596, doi:DOI:10.1016/j.ijsolstr.2004.05.029. URL http://www.sciencedirect.com/science/article/pii/S0020768304002562.
79. Papadrakakis M. A method for the automatic evaluation of the dynamic relaxation parameters. *Computer Methods in Applied Mechanics and Engineering* 1981; **25**(1):35 – 48, doi:DOI:10.1016/0045-7825(81)90066-9. URL http://www.sciencedirect.com/science/article/pii/0045782581900669.
80. Rice J. *Mathematical analysis in the mechanics of fracture*, vol. 2. IN H. Liebotwitz, 1968.

81. Chao TW, Shepherd JE. Fracture response of externally flawed aluminum cylindrical shells under internal gaseous detonation loading. *International Journal of Fracture* 2005; **134**:59–90. URL http://dx.doi.org/10.1007/s10704-005-5462-x, 10.1007/s10704-005-5462-x.
82. Oakley DR, Knight NF. Adaptive dynamic relaxation algorithm for non-linear hyperelastic structures part i. formulation. *Computer Methods in Applied Mechanics and Engineering* 1995; **126**(1-2):67 – 89, doi:DOI: 10.1016/0045-7825(95)00805-B. URL http://www.sciencedirect.com/science/article/pii/004578259500805B.
83. Zhang L, Kadkhodayan M, Mai YW. Development of the madr method. *Computers & Structures* 1994; **52**(1):1 – 8, doi:DOI:10.1016/0045-7949(94)90249-6. URL http://www.sciencedirect.com/science/article/pii/0045794994902496.

A. LINEARIZATION OF MEMBRANE COMPATIBILITY TERM

This appendix describes the establishment of $\delta\left(\bar{j}\boldsymbol{n}^{\alpha}\right)$ which appears in the compatibility membrane term (see equation (43)). As the shearing is neglected for Kirchhoff-Love shell,

$$\boldsymbol{n}^{\alpha} = \left(\tilde{n}^{\alpha\beta} + \lambda_{\mu}^{\beta}\tilde{m}^{\alpha\mu}\right)\boldsymbol{\varphi}_{,\beta}\,, \tag{91}$$

with,

$$\lambda_{\mu}^{\beta} = \lambda_h \boldsymbol{t}_{,\mu}\cdot\boldsymbol{\varphi}^{,\beta}\,. \tag{92}$$

The virtual form can therefore be computed as,

$$\begin{aligned}\delta\left(\bar{j}\boldsymbol{n}^{\alpha}\right) &= \delta\left[\bar{j}\left(\tilde{n}^{\alpha\beta} + \lambda_{\mu}^{\beta}\tilde{m}^{\alpha\mu}\right)\boldsymbol{\varphi}_{,\beta}\right] = \delta\left(\bar{j}\tilde{n}^{\alpha\beta} + \bar{j}\lambda_{\mu}^{\beta}\tilde{m}^{\alpha\mu}\right)\boldsymbol{\varphi}_{,\beta} + \bar{j}\left(\tilde{n}^{\alpha\beta} + \lambda_{\mu}^{\beta}\tilde{m}^{\alpha\mu}\right)\delta\boldsymbol{\varphi}_{,\beta}\\ &= \delta\left(\bar{j}\tilde{n}^{\alpha\beta}\right)\boldsymbol{\varphi}_{,\beta} + \bar{j}\tilde{m}^{\alpha\mu}\delta\lambda_{\mu}^{\beta}\boldsymbol{\varphi}_{,\beta} + \lambda_{\mu}^{\beta}\delta\left(\bar{j}\tilde{m}^{\alpha\mu}\right)\boldsymbol{\varphi}_{,\beta} + \\ &\quad \bar{j}\left(\tilde{n}^{\alpha\beta} + \lambda_{\mu}^{\beta}\tilde{m}^{\alpha\mu}\right)\boldsymbol{\varphi}_{,\gamma}\cdot\boldsymbol{\varphi}^{,\gamma}\delta\boldsymbol{\varphi}_{,\beta}\,,\end{aligned} \tag{93}$$

with the introduction of the identity $\boldsymbol{\varphi}_{,\gamma}\cdot\boldsymbol{\varphi}^{,\gamma} = 1$ in the last term. Then, the values of $\delta\tilde{n}^{\alpha\beta}$ and $\delta\tilde{m}^{\alpha\mu}$ can be computed by linearization:

$$\tilde{n}^{\alpha\beta} = \frac{\bar{j}_0}{2\bar{j}}\mathcal{H}_n^{\alpha\beta\gamma\delta}\left(\boldsymbol{\varphi}_{,\gamma}\cdot\boldsymbol{\varphi}_{,\delta} - \boldsymbol{\varphi}_{0,\gamma}\cdot\boldsymbol{\varphi}_{0,\delta}\right)\,, \tag{94}$$

$$\tilde{m}^{\alpha\mu} = \frac{\bar{j}_0}{\lambda_h\bar{j}}\mathcal{H}_m^{\alpha\mu\gamma\delta}\left(\boldsymbol{\varphi}_{,\gamma}\cdot\boldsymbol{t}_{,\delta} - \boldsymbol{\varphi}_{0,\gamma}\cdot\boldsymbol{t}_{0,\delta}\right)\,, \tag{95}$$

which gives,

$$\begin{aligned}\delta\left(\bar{j}\boldsymbol{n}^{\alpha}\right) &= \frac{\bar{j}_0}{2}\mathcal{H}_n^{\alpha\beta\gamma\delta}\left(\delta\boldsymbol{\varphi}_{,\gamma}\cdot\boldsymbol{\varphi}_{,\delta} + \boldsymbol{\varphi}_{,\gamma}\cdot\delta\boldsymbol{\varphi}_{,\delta}\right)\boldsymbol{\varphi}_{,\beta} + \bar{j}\boldsymbol{n}^{\alpha}\cdot\boldsymbol{\varphi}^{,\beta}\delta\boldsymbol{\varphi}_{,\beta}\\ &+ \frac{\bar{j}_0}{\lambda_h}\lambda_{\mu}^{\beta}\mathcal{H}_m^{\alpha\mu\gamma\delta}\left(\delta\boldsymbol{\varphi}_{,\gamma}\cdot\boldsymbol{t}_{,\delta} + \boldsymbol{\varphi}_{,\gamma}\cdot\delta\boldsymbol{t}_{,\delta}\right)\boldsymbol{\varphi}_{,\beta} + \bar{j}\tilde{m}^{\alpha\mu}\delta\lambda_{\mu}^{\beta}\boldsymbol{\varphi}_{,\beta}\,.\end{aligned} \tag{96}$$

Moreover using equation (92),

$$\delta\lambda_{\mu}^{\beta} = \lambda_h\left(\delta\boldsymbol{t}_{,\mu}\cdot\boldsymbol{\varphi}^{,\beta} + \boldsymbol{t}_{,\mu}\cdot\delta\boldsymbol{\varphi}^{,\beta}\right)\,. \tag{97}$$

Prepared using nmeauth.cls
DOI: 10.1002/nme

The second member of this equation can be rewritten (to remove $\delta\boldsymbol{\varphi}^{,\beta}$) using successively

$$\begin{aligned}
\delta\left(\boldsymbol{\varphi}^{,\alpha}\cdot\boldsymbol{\varphi}_{,\beta}\right) &= 0\,, && (98)\\
\delta\boldsymbol{\varphi}^{,\alpha}\cdot\boldsymbol{\varphi}_{,\beta} &= -\boldsymbol{\varphi}^{,\alpha}\cdot\delta\boldsymbol{\varphi}_{,\beta}\,, && (99)\\
\boldsymbol{t}_{,\alpha}\cdot\delta\boldsymbol{\varphi}^{,\beta} &= \frac{\lambda_\alpha^\mu}{\lambda_h}\boldsymbol{\varphi}_{,\mu}\cdot\delta\boldsymbol{\varphi}^{,\beta} = -\frac{\lambda_\alpha^\mu}{\lambda_h}\boldsymbol{\varphi}^{,\beta}\delta\boldsymbol{\varphi}_{,\mu}\,, && (100)
\end{aligned}$$

leading to

$$\delta\lambda_\mu^\beta = \lambda_h\left(\delta\boldsymbol{t}_{,\mu}\cdot\boldsymbol{\varphi}^{,\beta} - \frac{\lambda_\mu^\zeta}{\lambda_h}\boldsymbol{\varphi}^{,\beta}\cdot\delta\boldsymbol{\varphi}_{,\zeta}\right)\,. \tag{101}$$

Finally (96) becomes

$$\begin{aligned}
\delta\left(\bar{j}\boldsymbol{n}^\alpha\right) &= \frac{\bar{j}_0}{2}\mathcal{H}_n^{\alpha\beta\gamma\delta}\left(\delta\boldsymbol{\varphi}_{,\gamma}\cdot\boldsymbol{\varphi}_{,\delta}+\boldsymbol{\varphi}_{,\gamma}\cdot\delta\boldsymbol{\varphi}_{,\delta}\right)\boldsymbol{\varphi}_{,\beta} + \bar{j}\boldsymbol{n}^\alpha\cdot\boldsymbol{\varphi}^{,\beta}\delta\boldsymbol{\varphi}_{,\beta}\\
&+ \frac{\bar{j}_0}{\lambda_h}\lambda_\mu^\beta\mathcal{H}_m^{\alpha\mu\gamma\delta}\left(\delta\boldsymbol{\varphi}_{,\gamma}\cdot\boldsymbol{t}_{,\delta}+\boldsymbol{\varphi}_{,\gamma}\cdot\delta\boldsymbol{t}_{,\delta}\right)\boldsymbol{\varphi}_{,\beta}\\
&+ \bar{j}\lambda_h\tilde{m}^{\alpha\mu}\left(\delta\boldsymbol{t}_{,\mu}\cdot\boldsymbol{\varphi}^{,\beta} - \frac{\lambda_\mu^\zeta}{\lambda_h}\boldsymbol{\varphi}^{,\beta}\cdot\delta\boldsymbol{\varphi}_{,\zeta}\right)\boldsymbol{\varphi}_{,\beta}\,, \qquad (102)
\end{aligned}$$

with $\tilde{m}^{\alpha\mu}=\tilde{\boldsymbol{m}}^\alpha\cdot\boldsymbol{\varphi}^{,\mu}$. This expression can be used for the implementation of $a_{nI2}^s(\boldsymbol{\varphi}_h,\delta\boldsymbol{\varphi})$ (43).

B. DYNAMIC RELAXATION

The principle of dynamic relaxation, introduced by Papadrakakis [79], is to annihilate the dynamic effect by the introduction of damping on the velocity field in such a way that the static solution is reached for a minimum of time steps[‖]. One interest of this method in this paper is to prescribe an initial load without dynamic effect and without the inversion of a stiffness matrix. Indeed, as for fracture very thin meshes are needed to capture crack phenomena, it leads to very large systems for which the inversion of stiffness matrix can be prohibitive. Furthermore, it allows an easy implementation to switch to a dynamic explicit analysis compared to an implicit initialization.

From developments of several authors [79, 82, 83], the dynamic relaxation can be generalized to the Hulbert-Chung algorithm [65] by introducing a damping factor c in the velocity equation. This modification is the only one in the algorithm, which allows an easy implementation and facilitates the switch between the two schemes. The computation of the damping factor is based on works of Zhang *et al.* [83] except that we compute a global damping factor and not a local damping factor by nodes as suggested in [83]. The reason of using a global damping factor is related to our implementation. Indeed as we used a dof manager to create dofs independently of nodes, it is very complex (and time consuming) to identify the three displacements related to a node. Nevertheless, the idea of Zhang *et al.* is used as it avoids to compute the stiffness matrix.

[‖] In fact, the static solution is reached after a bit longer than one fundamental period of the problem.

DOI: 10.1002/nme

Keeping these considerations in mind the value chosen for damping factor is,

$$\mathrm{c}^{\,n+1} \;=\; \frac{1}{1+2\xi_{n+1}\Delta t} \text{ with } \xi_{n+1} = \frac{\boldsymbol{x}^n \cdot \boldsymbol{F}^n_{\text{int}}}{\boldsymbol{x}^n \cdot \mathbf{M} \cdot \boldsymbol{x}^n}\,, \tag{103}$$

where $\boldsymbol{x}^n$ and $\boldsymbol{F}^n_{\text{int}}$ are respectively the nodal positions and internal forces at time n, and where $\mathbf{M}$ is the diagonalized mass matrix. In this work Δt is equal to the value of time step determined for the explicit Hulbert-Chung scheme. Indeed, for the application of an external force, the convergence depends on the fundamental period of the problem. Therefore an increase of density has no influence on the convergence as an augmentation of the time step involves the same increase of the fundamental period (*i.e.* the number of time steps needed to achieve convergence is the same no matter the time step value). The external force is applied at the beginning of simulation and is kept constant until convergence, which is based on the criterion (at iteration $n+1$),

$$\frac{\|\boldsymbol{F}_{\text{ext}} - \boldsymbol{F}^{n+1}_{\text{int}}\|}{\|\boldsymbol{F}_{\text{ext}} + \boldsymbol{F}^{n+1}_{\text{int}}\|} \;\leq\; e_{\text{tol}}\,, \tag{104}$$

where $\boldsymbol{F}_{\text{ext}}$ is the vector of external forces prescribed and where e_{tol} is a convergence parameter. A value of 10^{-3} seems to give accurate results with a minimal computational effort. Notice that this scheme can be easily used for parallel computation by calculating the scalar vector product on each processor before summing the different values.

DOI: 10.1002/nme